Generation of surface waves by shear-flow instability

W. R. Young† and C. L. Wolfe

Scripps Institution of Oceanography, La Jolla, CA 92093-0213, USA

We consider the linear stability of an inviscid parallel shear flow of air over water with gravity and capillarity. The velocity profile in the air is monotonically increasing upwards from the sea surface and is convex, while the velocity in the water is monotonically decreasing from the surface and is concave. An archetypical example, the 'double-exponential' profile, is solved analytically and studied in detail. We show that there are two types of unstable mode which can, in some cases, co-exist. The first type is the 'Miles mode' resulting from a resonant interaction between a surface gravity wave and a critical level in the air. The second unstable mode is an interaction between surface gravity waves and a critical level in the water, resulting in the growth of ripples. The gravity–capillary waves participating in this second resonance have negative intrinsic phase speed, but are Doppler shifted so that their actual phase speed is positive, and matches the speed of the base-state current at the critical level. In both cases, the Reynolds stresses of an exponentially growing wave transfer momentum from the vicinity of the critical level to the zone between the crests and troughs of a surface wave.

Key words: capillary waves, critical layers, waves/free-surface flows

1. Introduction

The windy generation of ocean surface waves – with wavelengths between millimetres and hundreds of metres – is a central problem in physical oceanography. The early investigations of Miles (1957, 1962) viewed wave growth as an exponentially growing instability on a pre-exisiting shear flow in an atmosphere above a still ocean. A more complete model includes a shear flow in the water as a representation of the wind-drift layer just below the sea surface: see figure 1 and Valenzuela (1976). Experimental evidence reinforced the hypothesis that wave growth is via an exponentially growing mode of instability that amplifies initial small wavelets (e.g. Kawai 1979). Following these pioneering works, attention has been focused on the normal modes of instability of a unidirectional sheared flow, $U(z)$, along the axis of x, with a base-state density profile

$$\rho(z) \stackrel{\text{def}}{=} \begin{cases} \rho_a & \text{if } z > 0, \\ \rho_w & \text{if } z < 0. \end{cases} \tag{1.1}$$

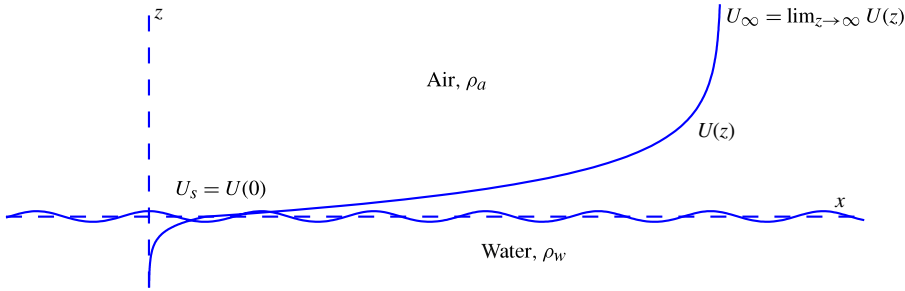† Email address for correspondence: wryoung@ucsd.edu

FIGURE 1. (Colour online) The coupled shear flow with the 'double-exponential' velocity profile in (4.1). Following Valenzuela (1976), the shear flow extends into the water with a shallow 'wind-drift' layer.

The subscripts 'a' and 'w' refer to air and water, and typically $\rho_w/\rho_a \approx 820$. The references in the upper block of table 1 are directed at this problem of wave generation by wind.

On the other hand, starting perhaps with Stern & Adam (1974), there is a second and larger stream of work directed mainly at understanding the generation of ripples by a shear-flow instability strictly within the wind-drift layer. (Following Lighthill (1978), 'ripples' are surface waves with length less than ~ 7 cm.) This second stream is summarized in the lower block of table 1. In this literature the dynamics of air is usually ignored by setting $\rho_a = 0$.

Lighthill (1962) gave a physical interpretation of the Miles mode: the air shear flow is perturbed by a free-surface wave, and the perturbation in the air grows most rapidly in the vicinity of a critical level at an altitude $z_c > 0$. The Miles instability relies crucially on transfer of energy and momentum from the critical level to the surface wave; the growth rate of the Miles instability is linearly proportional to the small parameter ρ_a/ρ_w.

Critical-level dynamics also plays a crucial role in the rippling instability of Stern & Adam (1974). But in this case the critical level is in the water at a depth $z_c < 0$. The critical-layer interaction involves surface waves with negative intrinsic phase speed that are Doppler shifted so that they travel in the same direction as the wind. A necessary condition for this strong Doppler shifting, and therefore a necessary condition for rippling instability, is that

$$U_s > c_{min}, \tag{1.2}$$

where U_s is the surface speed in figure 1 and $c_{min} \approx 23$ cm s^{-1} is the minimum speed of capillary–gravity waves. We show that if (1.2) is satisfied then the growth rate of the rippling instability can be very much larger than that of the Miles instability, and is insensitive to the dynamics of air, e.g. the rippling instability exists even if $\rho_a = 0$.

We caution that experimental evidence shows ripples amplifying on accelerating wind-driven surfaces even though U_s is less than c_{min} (Veron & Melville 2001). This point seems not to have been fully appreciated in the theoretical literature and we dwell further on it in the conclusion.

Another important point, which is not immediately clear from this literature, is that the shear flow in figure 1 supports the two different modes of instability described above. To our knowledge, only Caponi *et al.* (1992) have attempted to understand the co-existence of these two different modes of instability. One of our goals is to

Citation	Orr–Sommerfeld or Rayleigh?	Air?	Wind-drift layer?	Rippling instability discussed?	Miles instability discussed?
Valenzuela (1976)	OS	Yes	Yes	No	Yes
Kawai (1979)	OS	Yes	Yes	No	Yes
van Gastel, Janssen & Komen (1985)	OS	Yes	Yes	No	Yes
Wheless & Csanady (1993)	OS	Yes	Yes	No	Yes
Zeisel, Stiassnie & Agnon (2008)	OS	Yes	Yes	Perhaps	Yes
Miles (1957)	R	Yes	No	No	Yes
Miles (1962)	OS	Yes	No	No	Yes
Stern & Adam (1974)	R	No	Yes	Yes	No
Morland, Saffman & Yuen (1991)	R	No	Yes	Yes	No
Caponi et al. (1991)	R	No	Yes	Yes	No
Caponi et al. (1992)	R	Yes	Yes	Yes	Yes
Morland & Saffman (1993)	R	Yes	No	No	Yes
Shrira (1993)	R	No	Yes	Yes	No
Longuet-Higgins (1998)	R	No	Yes	Yes	No
Miles (2001)	R	No	Yes	Yes	No
Zhang (2005)	R	No	Yes	Yes	No
Bakas & Ioannou (2009)	R	No	Yes	Yes	No
This work	R	Yes	Yes	Yes	Yes

TABLE 1. Survey of the model assumptions made by some theoretical papers on gravity–capillary wave generation. The references in the upper block of are directed at the problem of wave generation by wind; those in the lower block consider the generation of ripples by a shear-flow instability within the wind-drift layer. The third column refers to whether the paper includes the dynamics of air by considering $\rho_a \neq 0$. The fourth column refers to whether the paper includes a model of the wind-drift layer in the water.

give a unified account of both instabilities to better understand the different physical processes required by the different mode types. To this end we recapitulate and extend Lighthill's arguments in § 3.

In principle, the Miles instability can excite gravity waves with lengths greater than 1 m. The Miles instability is therefore important as a mechanism for generating long gravity waves in the open ocean (Hristov, Miller & Friehe 2003; Janssen 2004). However, with laboratory investigations in mind, most of the studies of the Miles mode in the upper block of table 1 have confined attention to wavelengths less than 10 cm, i.e. to ripples and their near neighbours. For these short laboratory waves, the critical level is very close to the water surface and usually lies within a viscous sublayer. In addition to viscosity, for these short waves one must deal with capillarity and the wind-drift layer. Thus the studies in the upper block of table 1 all solve the Orr–Sommerfeld equation in both air and water. Of necessity there are many non-dimensional control parameters, and even specification of the basic-state shear flow $U(z)$ can be arduous. It is difficult to get a good picture of the essential nature of the two unstable modes from numerical solutions of the Orr–Sommerfeld equation. Indeed, with the possible exception of Zeisel et al. (2008), the computational studies in the upper block of table 1 did not consider surface flows fast enough to satisfy (1.2)

and therefore did not encounter the rippling mode, even though the rippling mode can co-exist with the Miles mode on centimetre laboratory scales.

For simplicity in this work we ignore the effects of viscosity and focus instead on a detailed characterization of the inviscid instabilities resulting from the coupled air–water shear flow. For the Miles instability, neglect of viscosity requires that the critical level should be above the viscous sublayer.

We show that both the Miles mode and the rippling mode of instability can be exhibited and understood in detail using the simple 'double-exponential' model for the coupled shear flow in figure 1. Results based on the double-exponential velocity profile are likely to be representative of smooth monotonic ($U_z > 0$) shear flows which are concave ($U_{zz} > 0$) in the water and convex ($U_{zz} < 0$) in the air. These profiles do not have a proper inflection point ($U_{zz} = 0$) because U_{zz} changes discontinuously at the sea surface, where $\rho(z)$ is also discontinuous. If the surface were rigid, the flow would therefore be stable according to Rayleigh's inflection-point criterion. However Stern & Adam (1974) and Morland *et al.* (1991) have shown that free-surface shear flows without inflection points are unstable. Because of the free surface, and contrary to the conclusion of Yih (1972), Rayleigh's theorem does not apply. The stability problem posed by inflectional velocity profiles beneath a free surface admits an additional class of unstable 'inflectional' modes, for which see Dimas & Triantafyllou (1994), Longuet-Higgins (1998) and Engevik (2000).

In §2 we formulate the inviscid linear stability problem, which amounts to Rayleigh's equation in the air and in the water with a dynamic boundary condition at the sea surface. In §3 we obtain general results showing how a growing capillary–gravity wave modifies the basic-state shear flow via induction of an Eulerian mean flow at second order in wave amplitude. This analysis reveals some surprising aspects of the wave–mean interaction due to free-surface dynamics. In particular, a full understanding of the mean-flow induction requires accounting for the momentum in the region below the wave crests and above the troughs; to this end, we generalize the irrotational still-water no-air formula for the crest–trough momentum given by Phillips (1977). In §4 we specialize the stability problem to the double-exponential profile in (4.1) and solve the stability problem in terms of hypergeometric functions. Solution of the resulting dispersion relation immediately reveals both the Miles mode and the rippling mode. Section 5 is a detailed study of the rippling mode based on the mild approximation $\rho_a = 0$. We provide an analytic characterization of the stability boundary and with extensive computations document the main properties of the most rapidly growing mode throughout the parameter space. Section 6 develops an approximate solution of the rippling stability problem that compares well with the more exact results from §5. Good estimates of the growth rate and phase speed of unstable eigenmodes are obtained without recourse to hypergeometric functions. However the main advantage of this development is that it provides insight into interaction of ripples with vortical disturbances concentrated at a subsurface critical layer. Section 7 discusses the Miles instability and shows how the small growth rate of the Miles mode is obtained perturbatively from the general formulation of §2. Section 8 is the conclusion.

2. Formulation of the linear stability problem

The linearized inviscid equations of motion for incompressible two-dimensional perturbations on a base-state shear flow $U(z)$ are

$$\rho \left(u_t + U u_x + w U_z \right) = -p_x, \tag{2.1}$$

$$\rho \left(w_t + U w_x \right) = -p_z, \tag{2.2}$$

$$u_x + w_z = 0. \tag{2.3}$$

In (2.1) and (2.2), $p(x, z, t)$ is the disturbance pressure; the total pressure is

$$p_{total} = p_a - \rho(z)gz + p, \tag{2.4}$$

where p_a is the constant atmospheric pressure and g is gravitational acceleration.

The base-state shear flow is

$$U(z) \stackrel{\text{def}}{=} \begin{cases} U_a(z) & \text{if } z > 0, \\ U_w(z) & \text{if } z < 0. \end{cases} \tag{2.5}$$

To remove Kelvin–Helmholtz instabilities we limit attention to velocity profiles that are continuous at the undisturbed sea surface, $z = 0$, so that $U_a(0) = U_w(0) = U_s$. The linearized kinematic condition at $z = 0$ is

$$\left(\partial_t + U_s \partial_x \right) \eta = w_s, \tag{2.6}$$

where $w_s \stackrel{\text{def}}{=} w(x, 0, t)$ is the vertical velocity of the sea surface and $\eta(x, t)$ is the displacement.

The dynamic boundary condition at $z = 0$ is that the jump in p_{total} is balanced by the force of surface tension with coefficient T. This requirement determines the jump in disturbance pressure:

$$p(x, 0^+, t) - p(x, 0^-, t) = -(\rho_a + \rho_w) \left(g' - \gamma \partial_x^2 \right) \eta, \tag{2.7}$$

where

$$\gamma \stackrel{\text{def}}{=} \frac{T}{\rho_a + \rho_w}, \quad g' \stackrel{\text{def}}{=} g \frac{\rho_w - \rho_a}{\rho_w + \rho_a}. \tag{2.8}$$

2.1. *Streamfunction and vorticity*

We introduce a streamfunction ψ with the convention $(u, w) = (\psi_z, -\psi_x)$; the vorticity is

$$\zeta \stackrel{\text{def}}{=} u_z - w_x = \nabla^2 \psi. \tag{2.9}$$

Eliminating the pressure between (2.1) and (2.2), we have

$$\zeta_t + U \zeta_x + w U_{zz} = 0. \tag{2.10}$$

If $U_{zz} = 0$ we recover the irrotational case, $\zeta = 0$, as a solution of (2.10).

2.2. *The Rayleigh equation*

If the streamfunction is represented as a harmonic modal disturbance,

$$\psi(x, z, t) = \phi(c, k; z) e^{ik(x-ct)} + \text{c.c.}, \tag{2.11}$$

then the pressure p and the surface displacement η are expressed in terms of $\phi(c, k; z)$ as

$$p(x, z, t) = \rho [U_z \phi - (U - c)\phi_z] e^{ik(x-ct)} + \text{c.c.} \tag{2.12}$$

and

$$\eta(x, t) = -\frac{\phi(0)}{U_s - c} e^{ik(x-ct)} + \text{c.c.} \tag{2.13}$$

Kinematic surface tension	γ	7.2×10^{-5} m^3 s^{-2}
Acceleration due to gravity	g	9.8 m s^{-2}
Capillary–gravity wavenumber	$k_{min} = \sqrt{g'/\gamma}$	370 m^{-1}
Capillary–gravity wavelength	$\lambda_{min} = 2\pi/k_{min}$	0.017 m
Capillary–gravity phase speed	$c_{min} = (4\,g'\gamma)^{1/4}$	0.23 m s^{-1}
Capillary–gravity time scale	$(k_{min}c_{min})^{-1}$	0.0118 s
Density of air	ρ_a	1.25 kg m^{-3}
Density of seawater	ρ_w	1025 kg m^{-3}
Density ratio	ρ_w/ρ_a	820

TABLE 2. Numerical values of gravity–capillary parameters and other quantities.

In terms of $\phi(z)$, the vorticity equation (2.10) becomes the Rayleigh equation

$$\phi_{zz} - \left(k^2 + \frac{U_{zz}}{U - c} \right) \phi = 0. \tag{2.14}$$

We take $k > 0$, and $c = c_r + ic_i$ is a complex phase velocity.

Using (2.12) and (2.13), the $z = 0$ boundary condition in (2.7) can be written as

$$[\epsilon \, \Xi_a(c, k) + (1 - \epsilon) \Xi_w(c, k)] (c - U_s)^2 + S (c - U_s) - g' - \gamma k^2 = 0, \tag{2.15}$$

where

$$\Xi_a(c, k) \overset{\text{def}}{=} -\frac{\phi_z(c, k; 0^+)}{\phi(c, k; 0)}, \quad \Xi_w(c, k) \overset{\text{def}}{=} \frac{\phi_z(c, k; 0^-)}{\phi(c, k; 0)}. \tag{2.16}$$

Also in (2.15), the density-weighted jump in shear at the sea surface is

$$S \overset{\text{def}}{=} (1 - \epsilon) U_z \left(0^- \right) - \epsilon U_z \left(0^+ \right), \tag{2.17}$$

where

$$\epsilon \overset{\text{def}}{=} \frac{\rho_a}{\rho_a + \rho_w}; \tag{2.18}$$

ϵ is a crucial small non-dimensional parameter in what follows.

The modal stability problem consists of obtaining a decaying (as $z \to \pm\infty$) solution of the Rayleigh equation (2.14) and then evaluating the Ξ. With Ξ_a and Ξ_w in hand, one obtains the dispersion relation from the surface boundary condition (2.15).

The simplest example is $U(z) = 0$, so that $\phi = \exp(-k|z|)$ is the solution of (2.14). In this case $\Xi_w(c, k) = \Xi_a(c, k) = k$, and the well known gravity–capillary dispersion relation $c = \pm c_{gc}(k)$, with

$$c_{gc}(k) \overset{\text{def}}{=} \sqrt{\frac{g'}{k} + \gamma k}, \tag{2.19}$$

is quickly recovered from (2.15). The gravity–capillary phase speed c_{gc} has a minimum value $c_{min} = (4g'\gamma)^{1/4}$ at the wavenumber $k_{min} = \sqrt{g'/\gamma}$ (see table 2).

Before considering further examples with non-zero $U(z)$ we obtain some general results that shed light on the energetics of the instability and the failure of the inflection-point criterion.

3. Momentum and energy conservation laws

3.1. *Wave energy*

From the linearized equations of motion (2.1)–(2.3) we obtain the kinetic energy equation

$$\frac{\mathrm{d}}{\mathrm{d}t} \underbrace{\frac{1}{2} \iint \rho\,(u^2 + w^2)\ \mathrm{d}x\,\mathrm{d}z}_{\overset{\mathrm{def}}{=}\widetilde{KE}} + \iint \rho u w U_z\ \mathrm{d}x\,\mathrm{d}z = \int w_s \Delta p\ \mathrm{d}x, \tag{3.1}$$

where $w_s(x, t)$ is the vertical velocity of the surface and $\Delta p \overset{\mathrm{def}}{=} p(x, 0^+, t) - p(x, 0^-, t)$ is the jump in disturbance pressure. Further in (3.1), $\widetilde{KE}$ is the kinetic energy of the wave in both air and water. The right-hand side of (3.1) is the transfer of energy to the wavy surface. Using the surface boundary conditions (2.6) and (2.7), this transfer due to the correlation of the pressure jump Δp with surface velocity w_s can be written as

$$\frac{\mathrm{d}}{\mathrm{d}t}\widetilde{PE} = -\int w_s \Delta p\ \mathrm{d}x, \tag{3.2}$$

where the potential and surfacial energy of the wave is

$$\widetilde{PE} \overset{\mathrm{def}}{=} \frac{1}{2}(\rho_a + \rho_w) \int g\eta^2 + \gamma \eta_x^2\ \mathrm{d}x. \tag{3.3}$$

Combining (3.1) and (3.2) to eliminate $\int w_s \Delta p\ \mathrm{d}x$, we obtain the wave energy equation

$$\frac{\mathrm{d}\widetilde{E}}{\mathrm{d}t} + \iint \rho u w U_z\ \mathrm{d}x\,\mathrm{d}z = 0, \tag{3.4}$$

where $\widetilde{E} \overset{\mathrm{def}}{=} \widetilde{KE} + \widetilde{PE}$ is the total energy of the wave. If the flow $U(z)$ is unstable, so that $\widetilde{E}$ is increasing, then the Reynolds stress uw must be negatively correlated with shear $U_z > 0$. This negative correlation could be in either the air, or the water, or both.

3.2. *Acceleration of the mean flow and total momentum conservation*

Denote an x-average by an overline. For example, the mean-square displacement of the sea surface is

$$\overline{\eta^2} = \frac{1}{L}\int_0^L \eta^2\ \mathrm{d}x, \tag{3.5}$$

where L is a large length. Thus if $\mathscr{U}(z, t)$ is the second-order-in-amplitude modification of the base-state flow $U(z)$ – so that the total mean flow is $U(z) + \mathscr{U}(z, t)$ – then the mean x-momentum equation is

$$(\rho\mathscr{U})_t + (\rho\overline{uw})_z = 0. \tag{3.6}$$

Integrating (3.6) separately in the air and in the water, and adding these expressions gives

$$\frac{\mathrm{d}}{\mathrm{d}t}\int_{-\infty}^{\infty} \rho\mathscr{U}\ \mathrm{d}z + (\rho_a + \rho_w)\,\overline{w_s u_s} = 0, \tag{3.7}$$

where

$$u_s(x, t) \overset{\mathrm{def}}{=} (1 - \epsilon)u(x, 0^-, t) - \epsilon u(x, 0^+, t) \tag{3.8}$$

is effectively a tangential velocity at the free surface.

We obtain another expression for the free-surface correlation $\overline{w_s u_s}$ by considering the linearized x-momentum equation (2.1) evaluated on either side of the sea surface. Evaluating the jump gives

$$(\partial_t + U_s \partial_x) u_s + S w_s = \left(g \partial_x - \gamma \partial_x^3\right) \eta, \tag{3.9}$$

where S is the density-weighted jump in shear, defined in (2.17). Multiplying (3.9) by η, x-averaging, and combining this with the free-surface condition (2.6), one eventually obtains

$$\frac{\mathrm{d}\mathscr{J}_s}{\mathrm{d}t} = \overline{w_s u_s}, \tag{3.10}$$

where

$$\mathscr{J}_s \overset{\text{def}}{=} \tfrac{1}{2} S \overline{\eta^2} + \overline{\eta u_s}; \tag{3.11}$$

$\mathscr{J}_s$ is the mean momentum density of the air and water in the zone below the wave crests and above the troughs. The expression in (3.11) generalizes the irrotational still-water no-air formula given by Phillips (1977).

We summarize these considerations by saying that to order amplitude-squared,

$$\text{Eulerian mean flow} = U(z) + \mathscr{U}(z, t) + \mathscr{J}_s(t)\delta(z). \tag{3.12}$$

Using (3.11), the strength of the sea-surface singularity, $\mathscr{J}_s(t)$, can be evaluated using only first-order-in-amplitude quantities obtained, for instance, from the solution of the Rayleigh equation.

Eliminating $\overline{w_s u_s}$ between (3.7) and (3.10) provides total momentum conservation in the form

$$\frac{\mathrm{d}}{\mathrm{d}t} \left(\int_{-\infty}^{\infty} \rho \mathscr{U} \, \mathrm{d}z + (\rho_a + \rho_w) \mathscr{J}_s \right) = 0. \tag{3.13}$$

The conserved quantity $\int \rho \mathscr{U} \, \mathrm{d}z + (\rho_a + \rho_w) \mathscr{J}_s$, is the momentum of the wavy disturbance, correct to second order in amplitude. If waves grow, starting with very small amplitude at an initial time, then time integration of (3.13) gives

$$\int_{-\infty}^{\infty} \rho \mathscr{U} \, \mathrm{d}z + (\rho_a + \rho_w) \mathscr{J}_s = 0. \tag{3.14}$$

The mean flows associated with the exponentially growing unstable modes found later in this paper satisfy (3.14).

3.3. *Pseudomomentum*

Following Taylor (1915), another expression for the surface Reynolds stress $\overline{w_s u_s}$ is obtained by multiplying the vorticity equation (2.10) by $\rho\zeta$ and averaging. If the base-state shear flow $U(z)$ has no inflection points then, using the Taylor identity

$$\overline{w\zeta} = (\overline{uw})_z, \tag{3.15}$$

the result can be written as

$$\left(\frac{\rho \overline{\zeta^2}}{2U_{zz}} \right)_t + (\rho uw)_z = 0. \tag{3.16}$$

The quantity $\overline{\zeta^2}/2U_{zz}$ is the Eulerian pseudomomentum density of the wave (Bühler 2009). Eliminating the Reynolds stress divergence between (3.6) and (3.16) we obtain

$$\frac{\mathrm{d}}{\mathrm{d}t}\left(\rho\mathscr{U} - \frac{\rho\overline{\zeta^2}}{2U_{zz}}\right) = 0. \tag{3.17}$$

If waves grow, starting with very small amplitude at an initial time, then time integration of (3.17) shows that the induced mean flow on either side of the sea surface is related to the disturbance vorticity by

$$\mathscr{U} = \frac{\overline{\zeta^2}}{2U_{zz}}. \tag{3.18}$$

Substituting (3.18) into (3.14), we write disturbance momentum conservation so that the sign of the various terms is made clear:

$$\frac{\rho_w}{2}\int_{-\infty}^{0}\frac{\overline{\zeta^2}}{|U_{zz}|}\,\mathrm{d}z - \frac{\rho_a}{2}\int_{0}^{\infty}\frac{\overline{\zeta^2}}{|U_{zz}|}\,\mathrm{d}z + (\rho_a + \rho_w)\mathscr{J}_s = 0. \tag{3.19}$$

The $|U_{zz}|$ arise, because, as indicated in figure 1, we are considering basic states with $U_{zz} > 0$ in the water and $U_{zz} < 0$ in the air. The disturbance momentum equation (3.19) shows how an unstable mode can grow spontaneously from infinitesimal amplitude without changing the net momentum of the fluid.

Because of the term $(\rho_a + \rho_w)\mathscr{J}_s$ in (3.19), one cannot conclude that momentum lost by the air above the crests is transmitted to the water beneath the troughs. Explicit solutions of the linearized stability in later sections will show that the crest–trough recoil, $\mathscr{J}_s$, is always important in the total momentum balance. In fact, in the Miles instability, the dominant balance in (3.19) is between the second and third terms: the air flow loses momentum which is transmitted to the crest–trough zone; there is no acceleration of the water below the troughs. And in the rippling instability the dominant balance in (3.19) is between the first and third terms: momentum is transferred from the crest–trough zone to the ocean below the troughs; air plays no role. Thus the disturbance momentum equation (3.19) provides a neat classification of the two unstable modes.

3.4. *Total energy conservation*

Multiplying the mean-flow equation (3.6) by $U(z)$, integrating over both air and water, and using earlier expressions for E_w and $\mathscr{J}_s$, one obtains the total energy conservation law

$$\frac{\mathrm{d}}{\mathrm{d}t}\left(\int_{-\infty}^{\infty}\rho\,U\,\mathscr{U}\,\mathrm{d}z + (\rho_a + \rho_w)U_s\mathscr{J}_s + \widetilde{E}\right) = 0. \tag{3.20}$$

The combination $\int \rho\,U\,\mathscr{U}\,\mathrm{d}z + (\rho_a + \rho_w)U_s\mathscr{J}_s$ on the left of (3.20) can be interpreted by squaring the total mean velocity in (3.12) and integrating in z to obtain the kinetic energy of the mean flow as

$$\int_{-\infty}^{\infty}\frac{1}{2}\rho U^2\,\mathrm{d}z + \underbrace{\int_{-\infty}^{\infty}\rho\,U\mathscr{U}\,\mathrm{d}z + (\rho_a + \rho_w)U_s\mathscr{J}_s}_{=O(a^2)} + O(a^3). \tag{3.21}$$

If the disturbance amplifies spontaneously with infinitesimal initial amplitude, then the total energy of the disturbance is zero, i.e. the $O(a^2)$ terms on the right of (3.21) are

zero. To emphasize the definite sign of some terms in the disturbance energy, we use (3.18) to write this requirement as

$$\frac{\rho_w}{2} \int_{-\infty}^{0} \frac{\zeta^2 U}{|U_{zz}|} \, \mathrm{d}z - \frac{\rho_a}{2} \int_{0}^{\infty} \frac{\zeta^2 U}{|U_{zz}|} \, \mathrm{d}z + (\rho_a + \rho_w) U_s \mathscr{J}_s + \widetilde{E} = 0. \qquad (3.22)$$

On the left-hand side above, only the crest–trough energy density, $U_s \mathscr{J}_s$, has indefinite sign.

The disturbance energy equation (3.22) is analogous to the disturbance momentum equation (3.19): in both relations there is the crest–trough momentum density $\mathscr{J}_s$ with indefinite sign. However, one can linearly combine (3.22) with (3.19) to eliminate $\mathscr{J}_s$ and obtain the wave energy $\widetilde{E}$ as

$$\widetilde{E} = \int_{-\infty}^{\infty} \rho(U_s - U) \frac{\zeta^2}{2 U_{zz}} \, \mathrm{d}z. \qquad (3.23)$$

In the basic states under consideration here $(U_s - U)/U_{zz}$ is positive for all z, and (3.23) is a pure expression of the relation between the spontaneous growth of wave energy $\widetilde{E}$ and the Eulerian pseudomomentum $\overline{\zeta^2}/(2 U_{zz})$.

4. The double-exponential model

We now consider the 'double-exponential' base-state velocity profile

$$U(z) = \begin{cases} U_\infty - (U_\infty - U_s) \mathrm{e}^{-z/h_a} & \text{if } z > 0, \\ U_s \mathrm{e}^{z/h_w} & \text{if } z < 0. \end{cases} \qquad (4.1)$$

In this example the density-weighted jump in shear, defined in (2.17), is

$$S = (1 - \epsilon) \frac{U_s}{h_w} - \epsilon \frac{U_\infty - U_s}{h_a}. \qquad (4.2)$$

4.1. *The double-exponential dispersion relation*

The double-exponential has the advantage that the Rayleigh equation (2.14) can be solved exactly (Hughes & Reid 1965; Morland & Saffman 1993). In the air, the solution is

$$\phi(c, k; z > 0) = \mathrm{e}^{-kz} \frac{F\left(\alpha_a, \beta_a, 2\kappa_a + 1; \dfrac{U_\infty - U_s}{U_\infty - c} \mathrm{e}^{-z/h_a}\right)}{F\left(\alpha_a, \beta_a, 2\kappa_a + 1; \dfrac{U_\infty - U_s}{U_\infty - c}\right)}, \qquad (4.3)$$

where F is the Gaussian hypergeometric function

$$F(a, b, c; \xi) \overset{\mathrm{def}}{=} 1 + \frac{ab}{c} \frac{\xi}{1!} + \frac{a(a+1)b(b+1)}{c(c+1)} \frac{\xi^2}{2!} + \cdots \qquad (4.4)$$

and

$$\kappa_a \overset{\mathrm{def}}{=} k h_a, \quad \alpha_a \overset{\mathrm{def}}{=} \kappa_a - \sqrt{1 + \kappa_a^2}, \quad \beta_a \overset{\mathrm{def}}{=} \kappa_a + \sqrt{1 + \kappa_a^2}. \qquad (4.5)$$

This solution requires $c_i \neq 0$ so that the argument of the hypergeometric function in (4.3) does not lie on the branch line that runs along the real axis from $\xi = 1$ to ∞.

Likewise, the solution in the water is

$$\phi(c, k; z < 0) = e^{kz} \frac{F\left(\alpha_w, \beta_w, 2\kappa_w + 1; \dfrac{U_s}{c}\, e^{z/h_w}\right)}{F\left(\alpha_w, \beta_w, 2\kappa_w + 1; \dfrac{U_s}{c}\right)}, \tag{4.6}$$

with

$$\kappa_w \overset{\text{def}}{=} kh_w, \quad \alpha_w \overset{\text{def}}{=} \kappa_w - \sqrt{1 + \kappa_w^2}, \quad \beta_w \overset{\text{def}}{=} \kappa_w + \sqrt{1 + \kappa_w^2}. \tag{4.7}$$

Note that the α are negative, and $\alpha_a \beta_a = \alpha_w \beta_w = -1$.

Because the base-state velocity in figure 1 is continuous at the air–water interface $z = 0$, the amplitude function ϕ is also continuous at $z = 0$. In (4.3) and (4.6) we have implemented this condition and adopted the normalization $\phi(c, k; 0) = 1$.

The hypergeometric solutions above provide an exact description of the nearly singular flow at the critical level. The flow is nearly singular because small non-zero c_i ensures that the Rayleigh denominator $U(z) - c$ is non-zero at the critical level where $U(z_c) = c_r$. Non-zero c_i also ensures that ξ does fall on the real axis, i.e. the hypergeometric branch line is the analytic counterpart of the critical layer.

Using the differentiation identity for hypergeometric functions, we find that the Ξ defined in (2.16) are

$$\Xi_a(c, k) = k - \frac{1}{h_a(1 + 2\kappa_a)} \frac{U_\infty - U_s}{U_\infty - c} \frac{F\left(\alpha_a + 1, \beta_a + 1, 2\kappa_a + 2; \dfrac{U_\infty - U_s}{U_\infty - c}\right)}{F\left(\alpha_a, \beta_a, 2\kappa_a + 1; \dfrac{U_\infty - U_s}{U_\infty - c}\right)}, \tag{4.8}$$

$$\Xi_w(c, k) = k - \frac{1}{h_w(1 + 2\kappa_w)} \frac{U_s}{c} \frac{F\left(\alpha_w + 1, \beta_w + 1, 2\kappa_w + 2, \dfrac{U_s}{c}\right)}{F\left(\alpha_w, \beta_w, 2\kappa_w + 1, \dfrac{U_s}{c}\right)}. \tag{4.9}$$

The dispersion relation for the double-exponential profile is obtained by substituting S in (4.2) and the hypergeometric expressions in (4.8) and (4.9) into the boundary condition (2.15). The eigenrelation $c(k)$ is then obtained by numerical solution of the dispersion relation (which we accomplished in *Mathematica*). Typical solutions of the dispersion relation are shown in figures 2 and 3.

4.2. *The unstable modes*

Figure 2 shows that there are two different unstable modes. At low wavenumbers there is a slowly growing prograde mode, familiar as the classical wind-wave generation mechanism described by Miles (1957, 1962) and Janssen (2004). The growth rate of this long-wave instability is linearly proportional to ϵ in (2.18) and is therefore small. There is also a rapidly growing high-wavenumber retrograde mode resulting in the amplification of ripples. The growth rates and wavenumbers are so different that to make both unstable modes visible in figure 2 it is necessary to use a logarithmic scale. The unstable bands overlap at intermediate wavenumbers, but growth rates are extremely small in this overlap.

The properties of the retrograde rippling mode are not affected by changing the asymptotic air speed U_∞: all rippling curves in figures 1 and 2 coincide to within the
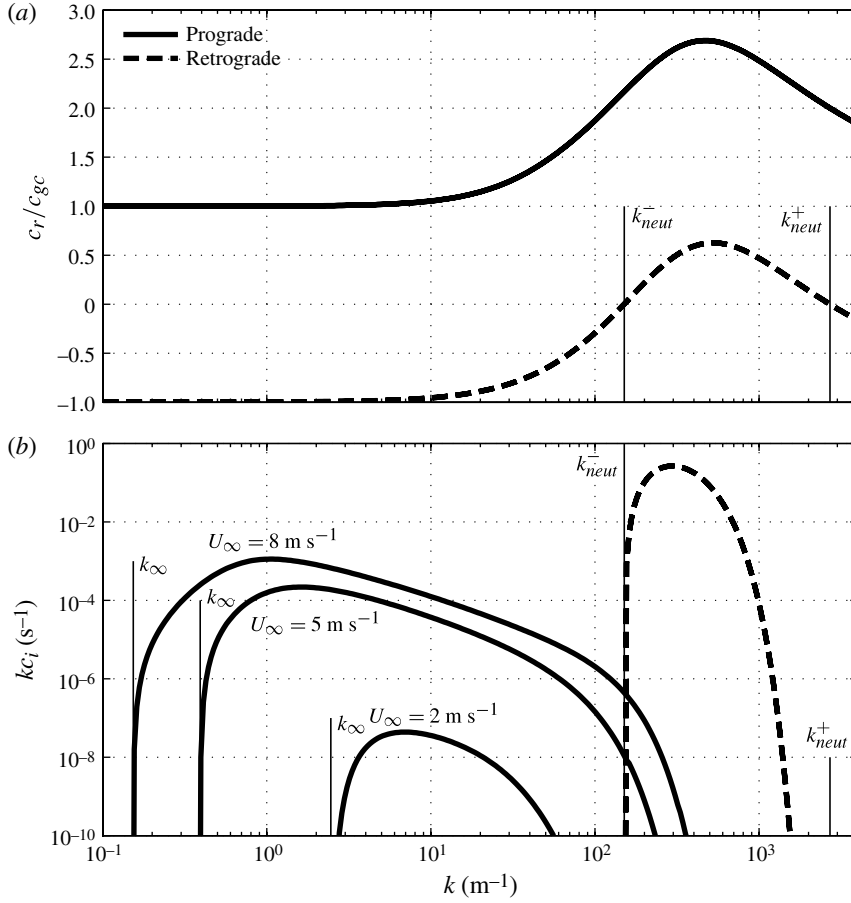
FIGURE 2. Three solutions of the dispersion relation (2.15) using the 'double-exponential' Ξ in (4.8) and (4.9). The three solutions for $c(k) = c_r(k) + \mathrm{i}c_i(k)$ correspond to $U_\infty = 2$, 5 and 8 m s^{-1}. (a) $c_r(k)$, normalized by the gravity–capillary speed $c_{gc}(k)$ in (2.19); the three cases coincide to within the line width. (b) The growth rate kc_i. The necessary condition for rippling instability in (4.10) is satisfied with $U_s = 2c_{min}$. For the high-wavenumber rippling instability (dashed), the three cases coincide to within the line width. On the other hand, the growth rate of the low-wavenumber Miles mode (solid) is sensitive to U_∞. In this illustration, the parameters in (4.1) are $U_s = 2c_{min} = 46$ cm s^{-1}, $h_a = 1$ m and $h_w = 2/k_{min} = 0.54$ cm.

line width as U_∞ varies from 2 to 8 m s^{-1}. Thus the rippling mode can be understood by neglecting the dynamics of air (see §§ 5 and 6).

Comparison of figure 2 with figure 3 shows that the result of reducing the surface speed U_s from $2c_{min}$ to $c_{min}/2$, while holding all other parameters fixed, is to eliminate the rippling instability. This elimination illustrates a main conclusion of Caponi *et al.* (1991): activation of the rippling instability requires

$$c_{min} < U_s, \qquad (4.10)$$

where $U_s = U(0)$ is the sea-surface velocity and $c_{min} \approx 23$ cm s^{-1} is the minimum phase speed of capillary–gravity waves in still water (see table 2). The rippling mode of instability results from destabilization of ripples propagating with intrinsic phase
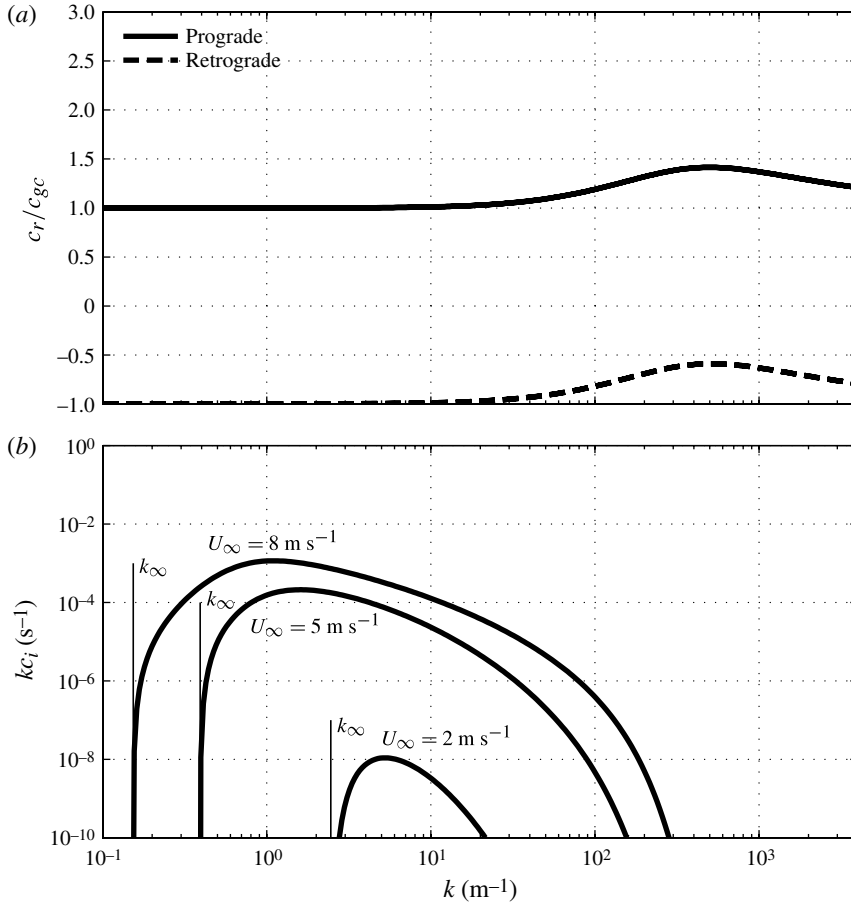
FIGURE 3. Three solutions of the dispersion relation (2.15) using the 'double-exponential' Ξ's in (4.8) and (4.9). The three solutions for $c(k) = c_r(k) + \mathrm{i}c_i(k)$ correspond to $U_\infty = 2$, 5 and 8 m s^{-1}. (a) $c_r(k)$, normalized by $c_{gc}(k)$ in (2.19); the three curves coincide to within the line width for both pro- and retrograde modes. (b) The growth rate kc_i. In this case, with $U_s = c_{min}/2$, there is no rippling instability. The parameters in (4.1) are $U_s = c_{min}/2 = 11.5$ cm s^{-1}, $h_a = 1$ m and $h_w = 2/k_{min} = 0.54$ cm.

speed $-c_{gc}(k)$, i.e. waves which in still water would propagate against the shear flow in the negative direction ('retrograde' modes). If (4.10) is satisfied then retrograde ripples can be Doppler shifted by the shear flow so that their actual phase velocity is slightly positive, and can therefore equal the flow speed in the water at a critical level depth $z_c < 0$ satisfying $U(z_c) = c_r$. This is the physical basis of the necessary condition for rippling instability in (4.10). The slowest ripples – those with wavenumbers close to k_{min} – are most vulnerable to Doppler shifting and thus the rippling instability is centred on k_{min}. These physical arguments are confirmed by a detailed solution in §5.

The air–water semicircle theorem proved by Morland & Saffman (1993) shows that waves with k less than

$$k_\infty \stackrel{\mathrm{def}}{=} \frac{g}{U_\infty^2} \qquad (4.11)$$

are stable. The wavenumber k_∞ is the low-wavenumber cut-off of the Miles instability and is indicated in figures 2 and 3. The physical basis of this condition is that the Miles mode results from the destabilization of a long gravity wave propagating with an intrinsic phase speed $+c_{gc}(k)$ (a 'prograde' mode). There is a resonant interaction between the irrotational wave velocity in the air and a critical level at an altitude $z_c > 0$ where $U(z_c) = c_r$. Waves with $k < k_\infty$ travel faster than the wind in (4.1) so that critical-level resonance is not possible: long and very fast gravity waves with $k < k_\infty$ are therefore stable. The Miles instability is discussed in greater detail in §7.

5. Rippling instability: $\epsilon = 0$

The cleanest separation of the two modes of instability in figure 2 is based on the small parameter $\epsilon = \rho_a/(\rho_a + \rho_w)$. In particular, the main properties of the retrograde rippling mode are unaffected by setting ϵ to zero. Thus in this section, and in the next, we focus on the retrograde rippling mode with $\epsilon = 0$. The solid curves in figure 4 show a survey of $\epsilon = 0$ solutions of the double-exponential dispersion relation as a function of the two control parameters

$$\bar{g} \stackrel{\text{def}}{=} \frac{gh_w}{U_s^2} \quad \text{and} \quad \bar{\gamma} \stackrel{\text{def}}{=} \frac{\gamma}{h_w U_s^2}. \tag{5.1}$$

With $\epsilon = 0$, $\bar{g}$ and $\bar{\gamma}$ are the only remaining control parameters characterizing rippling instability of the exponential velocity profile. Our goal is to understand the main features revealed by this survey of rippling instability in this two-parameter space.

5.1. *The high- and low-wavenumber cut-off wavenumbers of rippling instability: $c = 0$*

Morland *et al.* (1991) noticed that if $c = 0$ then there is an elementary solution of the water Rayleigh equation:

$$\phi_w(0, k; z) = e^{qz/h_w}, \tag{5.2}$$

where

$$q(k) \stackrel{\text{def}}{=} \sqrt{1 + \kappa_w^2}, \tag{5.3}$$

with $\kappa_w = h_w k$. This $c = 0$ and $\epsilon = 0$ solution locates the rippling stability boundary: the phase speed c_r is zero because the current has just managed to arrest the intrinsic propagation of the $-c_{gc}$ gravity–capillary wave. As U_s increases the arrest first occurs at a critical level located at $z = -\infty$, where both $U(z)$ and c_r are zero. As the current speed increases, the ripple is Doppler shifted so that it travels in the positive direction $c_r > 0$, and the critical level moves upwards towards $z = 0$. The growth rate of the rippling instability increases as the current speed (and vorticity gradient) at the critical level increases. Thus both c_r and c_i become positive close to the stability boundary defined by $c = 0$.

With the solution in (5.2), $\mathcal{Z}_w(c, k) = q/h_w$, and thus the $\epsilon = 0$ and $c = 0$ version of the dispersion relation (2.15) is

$$\sqrt{1 + \kappa_w^2} - 1 - \bar{g} - \bar{\gamma}\kappa_w^2 = 0, \tag{5.4}$$

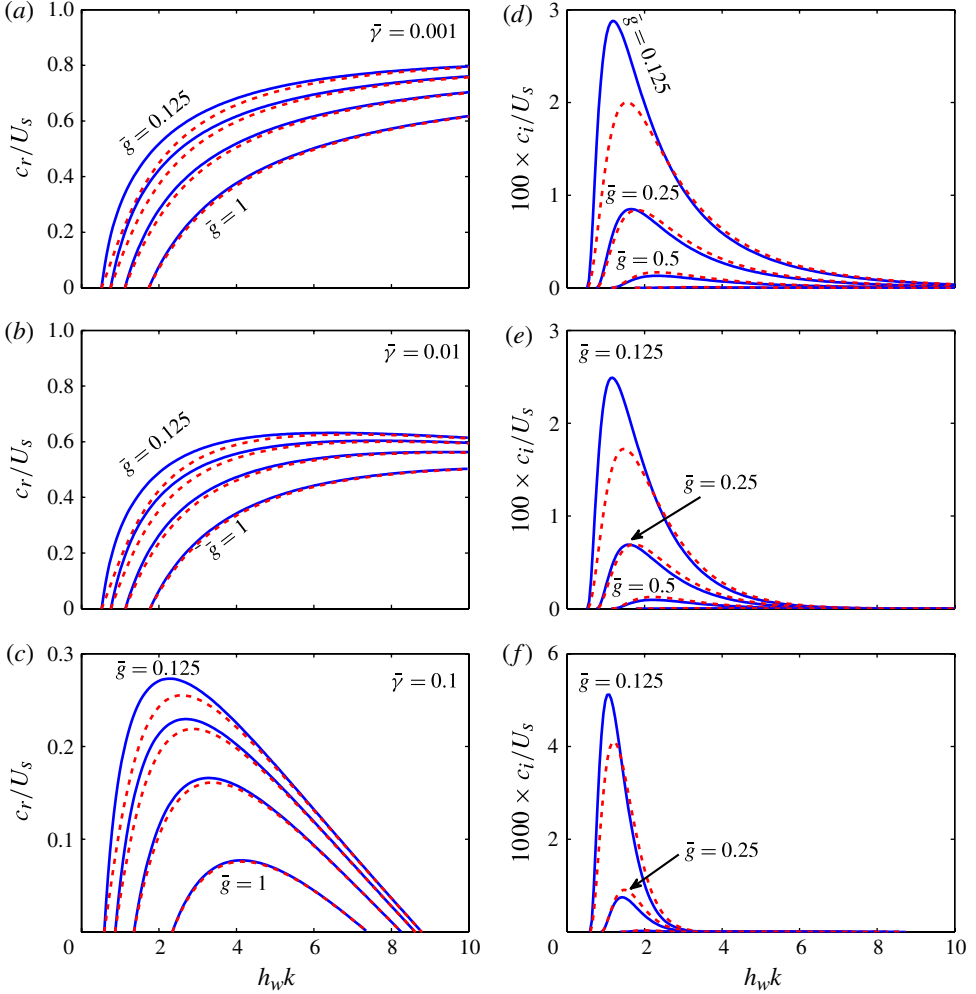where $\bar{g}$ and $\bar{\gamma}$ are the control parameters in (5.1).

FIGURE 4. (Colour online) (*a–c*) Solid curves show $c_r(k)$ determined from numerical solution of (2.15) with $\epsilon = 0$ and $\bar{g} = 0.125$, 0.25, 0.5 and 1 for (*a*) $\bar{\gamma} = 0.001$, (*b*) $\bar{\gamma} = 0.01$, and (*c*) $\bar{\gamma} = 0.1$. The dotted curves are the approximation to c_r by c_{sgc}^- in (6.3). (*d–f*) Solid curves show $c_i(k)$ corresponding to the solid curves in (*a–c*); $\bar{g} = 1$ is visible as a slight thickening of the abscissa in (*d,e*). Both $\bar{g} = 1$ and $\bar{g} = 0.5$ are visible as a slight thickening of the abscissa in (*f*). The dotted curves show the approximation to $c_i(k)$ obtained by taking the imaginary part of (6.14).

The two real solution of (5.4) for κ_w provide the high and low cut-off wavenumbers of the instability. These 'neutral' wavenumbers are therefore

$$h_w k_{neut}^{\pm}(\bar{g}, \bar{\gamma}) = \frac{1}{\bar{\gamma}} \sqrt{\frac{1}{2} - \bar{\gamma} - \bar{\gamma}\bar{g} \pm \sqrt{\left(\frac{1}{2} - \bar{\gamma}\right)^2 - \bar{g}\bar{\gamma}}}, \qquad (5.5)$$

and the rippling unstable range of wavenumbers is

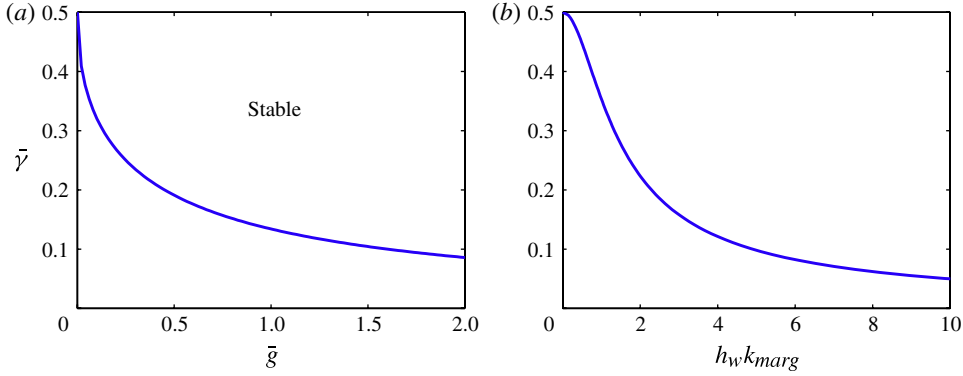$$k_{neut}^-(\bar{g}, \bar{\gamma}) < k < k_{neut}^+(\bar{g}, \bar{\gamma}). \qquad (5.6)$$

FIGURE 5. (Colour online) (*a*) The marginal curve, $\bar{\gamma} = (1 + \bar{g} - \sqrt{2\bar{g} + \bar{g}^2})/2$, is the stability boundary of the rippling mode in the $(\bar{g}, \bar{\gamma})$-parameter plane. (*b*) The wavenumber of incipiently unstable ripples, k_{marg} in (5.8), as a function of $\bar{\gamma}$.

These cut-off wavenumbers are indicated in figure 2(*b*): $k_{neut}^-(\bar{g}, \bar{\gamma})$ is the low-wavenumber cut-off of the rippling instability and $k_{neut}^+(\bar{g}, \bar{\gamma})$ is the high-wavenumber cut-off.

5.2. *The marginal curve*

Equation (5.5) provides an elementary characterization of the rippling unstable region of the $(\bar{g}, \bar{\gamma})$-parameter plane. Specifically, the cut-off wavenumbers $k_{neut}^\pm$ are real if and only if

$$\bar{\gamma} \leqslant \tfrac{1}{2}\left[1 + \bar{g} - \sqrt{2\bar{g} + \bar{g}^2}\right]. \tag{5.7}$$

The inequality above is a necessary and sufficient condition for rippling instability of the exponential profile with $\rho_a = 0$. The marginal curve in the $(\bar{g}, \bar{\gamma})$-parameter plane – the right-hand side of (5.7) – is shown in figure 5(*a*). On the marginal curve

$$k_{neut}^+ = k_{neut}^- = \underbrace{h_w^{-1}\sqrt{\frac{1}{4\bar{\gamma}^2} - 1}}_{\stackrel{\text{def}}{=} k_{marg}}. \tag{5.8}$$

The marginal wavenumber, k_{marg}, is show as a function of $\bar{\gamma}$ in figure 5(*b*).

Below the marginal curve, in the region characterized by the inequality (5.7), the wavenumbers k_{neut}^+ and k_{neut}^- are real and distinct, and the flow is unstable. In the strongly unstable part of the parameter space, far from the marginal curve in figure 5(*a*), $k_{neut}^- \ll k_{neut}^+$ so that the unstable band of wavenumbers is very wide. For example, if $\bar{\gamma} \to 0$, then expanding (5.5) gives

$$k_{neut}^- = h_w^{-1}\sqrt{\bar{g}(2 + \bar{g})} + O(\bar{\gamma}), \tag{5.9}$$

$$k_{neut}^+ = h_w^{-1}\left[\bar{\gamma}^{-1} - (1 + \bar{g})\right] + O(\bar{\gamma}). \tag{5.10}$$

The expressions above show that the width of the rippling band varies as $\bar{\gamma}^{-1}$ as $\bar{\gamma} \to 0$.

5.3. *Gravity–capillary units*

The control parameters $\bar{g}$ and $\bar{\gamma}$ in (5.1) are convenient for the analysis in § 6. But alternative control parameters, with some advantages in applications, are based on the wavenumber k_{min} at which gravity–capillary waves in still water have minimum phase speed c_{min} (see table 2). The alternative control parameters are

$$\hat{h}_w \stackrel{\text{def}}{=} h_w k_{min} = \sqrt{\frac{\bar{g}}{\bar{\gamma}}} \quad \text{and} \quad \hat{U}_s \stackrel{\text{def}}{=} \frac{U_s}{c_{min}} = \frac{1}{(4\bar{g}\bar{\gamma})^{1/4}}. \tag{5.11}$$

In terms of $\hat{U}_s$ and $\hat{h}_w$ the cut-off wavenumbers in (5.5) are

$$k_{neut}^{\pm} = k_{min} \sqrt{2\hat{U}_s^4 - 2\frac{\hat{U}_s^2}{\hat{h}_w} - 1 \pm 2\frac{\hat{U}_s^2}{\hat{h}_w}\sqrt{\left(\hat{U}_s^2 \hat{h}_w - 1\right)^2 - \hat{h}_w^2}}. \tag{5.12}$$

The necessary and sufficient conditions for instability are that

$$\hat{U}_s > 1 \quad \text{and} \quad \frac{1}{\hat{U}_s^2 - 1} \leqslant \hat{h}_w. \tag{5.13}$$

The wavenumber on the marginal curve, $\hat{h}_w = (\hat{U}_s^2 - 1)^{-1}$, is

$$k_{marg} = k_{min} \sqrt{2\hat{U}_s^2 - 1}. \tag{5.14}$$

Figure 6 shows the marginal curve, and contours of $k_{neut}^{\pm}/k_{min}$, in the $(\hat{U}_s, \hat{h}_w)$ parameter plane.

Using U_s/c_{min} and $h_w k_{min}$ as the control parameters has the advantage that one can see the effects of independently changing the profile parameters U_s and h_w. For example, if $U_s = 2c_{min} = 0.46$ m s^{-1} then from (5.13), the required depth for instability is $h_w = 1/(3k_{min}) \approx 0.9$ mm. If $h_w k_{min} = 0.5$ then incipient instability requires $U_s = \sqrt{3}c_{min} \approx 0.4$ m s^{-1}. It is gratifying that the exponential model produces simple analytic relations for the marginal condition.

The right-hand side of (5.14) is always greater than one, so that $k_{marg} > k_{min}$ and incipient instability is strictly within the capillary band. In other words, close to the marginal curve in figure 6, the unstable band of wavenumbers satisfies

$$k_{min} < k_{neut}^- < k < k_{neut}^+. \tag{5.15}$$

The 'capillary sliver' defined by the inequality above is the shaded region in figure 6. Within the sliver only capillary waves (with $\lambda < \lambda_{min}$) are unstable. Above and to the right of the sliver the low-wavenumber cut-off k_{neut}^- is a gravity wave and thus the range of unstable wavenumbers straddles k_{min}. Thus, according to the linear theory, a necessary condition for generation of waves longer than λ_{min} is that the control parameters $\hat{U}_s$ and $\hat{h}_w$ put the system above the shaded sliver in figure 6.

5.4. *Properties of the most unstable mode*

Extensive computations using the $\epsilon = 0$ hypergeometric dispersion relation are summarized in figure 7 by showing the main properties of the most unstable rippling mode. Figure 7(a) shows the real part of c, normalized by c_{min}. Figure 7(b) shows the growth rate of the most unstable mode. The growth rate is normalized by $k_{min}c_{min} \approx 85$ s^{-1}, so that the 0.025-contour in figure 7(b) is an e-folding time of about half a second: because the gravity–capillary time scale $(k_{min}c_{min})^{-1}$ is short, waves
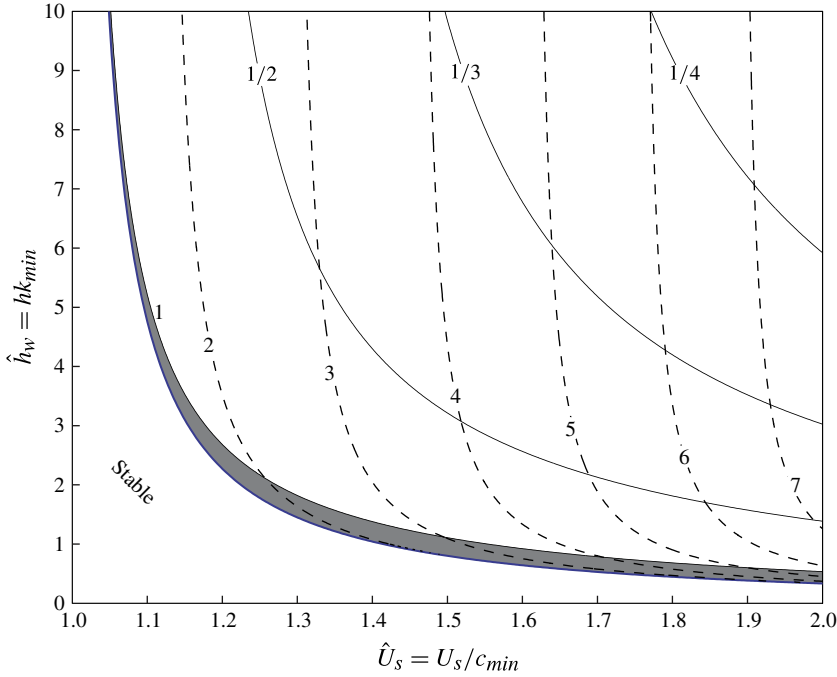
FIGURE 6. (Colour online) The marginal curve $\hat{h}_w = (\hat{U}_s^2 - 1)^{-1}$ and contours of k_{neut}^+/k_{min} (dashed) and k_{neut}^-/k_{min} (solid) in the $(\hat{U}_s, \hat{h})$-plane. The flow is stable below the marginal curve. In the shaded sliver both k_{neut}^+/k_{min} and k_{neut}^-/k_{min} are greater than one, i.e. the instability is totally within the capillary band. Note that solid curves corresponding to $k_{neut}^-/k_{min} > 1$ exist within the shaded sliver but are not shown.

with rather small non-dimensional growth rates still amplify quickly. The growth rate increases very rapidly with $\hat{U}_s$, and is less sensitive to variations in $\hat{h}_w$. Figure 7(c) shows the wavelength of the most unstable wave, normalized by $\lambda_{min} = 17$ mm. The most rapidly growing waves are close to the gravity–capillary transition. Figure 7(d) shows the ratio c_i/c_r, which equals the e-folding time of the most unstable wave, $1/(kc_i)$, multiplied by the frequency kc_r.

5.5. *Energy and momentum of unstable ripples*

Figure 8 shows the streamfunction and vorticity of an unstable rippling mode. The streamfunction in figure 8(a) is a slightly distorted version of the familiar irrotational streamfunction. Although the distortion is slight, the systematic tilt of the streamlines produces the vital Reynolds stress correlation $\overline{uw} < 0$: from the energy equation (3.3), $\overline{uw} < 0$ is required for a wave to extract energy from the shear flow with $U_z > 0$. Figure 8(b) shows the vorticity, $\zeta = \nabla^2 \psi$, and the small structure associated with the critical layer.

Figure 9 shows how the base-state shear flow, $U_s \exp(z/h_w)$, is modified by the Reynolds stress divergence of the growing wave in figure 8. As indicated by the argument surrounding (3.18), the below-trough Eulerian mean flow is accelerated at every depth. However the mean-flow acceleration is fastest within the critical layer where the disturbance vorticity is largest. This submarine acceleration is balanced by recoil in the zone above the wave troughs, i.e. by the surface density $\mathscr{I}_s$ in (3.13).
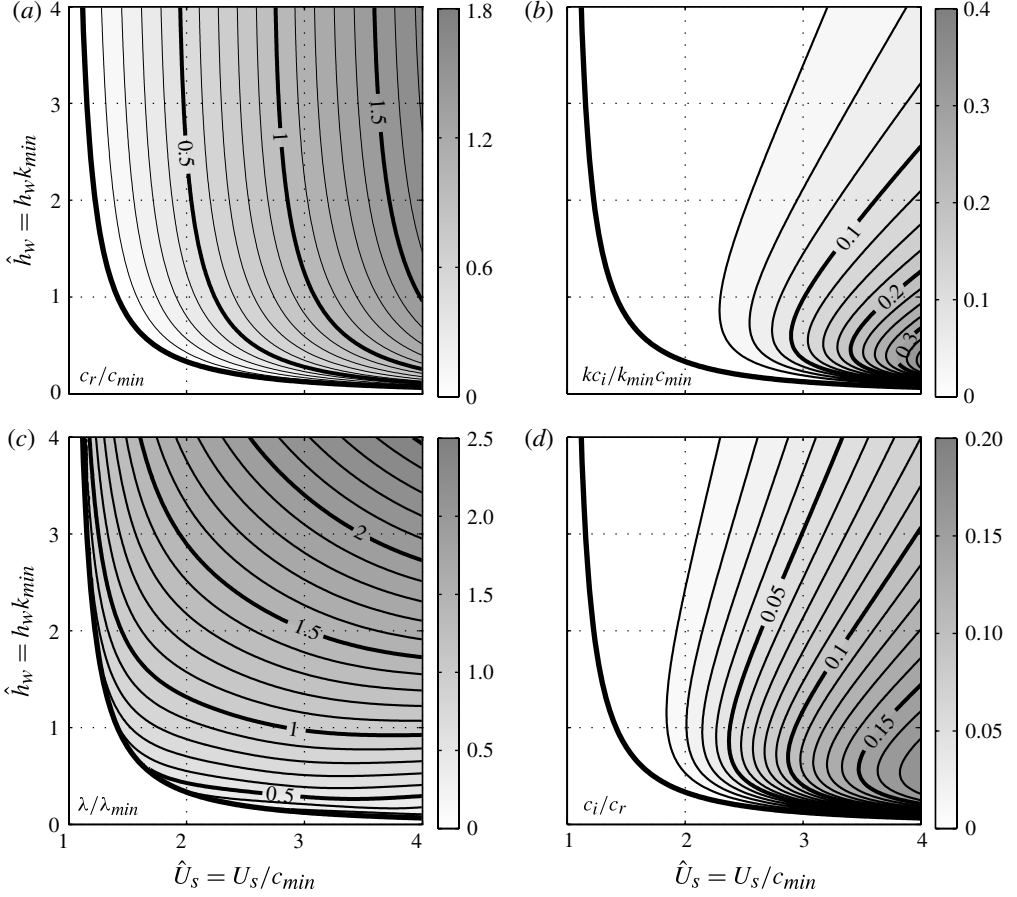
FIGURE 7. Properties of the most unstable rippling mode in the $(\hat{U}_s, \hat{h}_w)$ parameter plane; the thick curve is the stability boundary $\hat{h}_w = (\hat{U}_s^2 - 1)^{-1}$. (*a*) The real part of the phase speed scaled with $c_{min} = 0.23$ m s^{-1}. (*b*) Growth rate scaled with $k_{min}c_{min} = 85$ s^{-1}. (*c*) Wavelength of the most unstable wave scaled by $\lambda_{min} = 0.0170$ m. (*d*) The ratio c_i/c_r.

5.6. *Other wind-drift profiles, and cautionary comments on 'broken-line' profiles*

Without presenting the details here, we have shown that smooth concave water current profiles, with the same surface velocity and surface shear, have stability boundaries that are close to those of the exponential. That is, once the surface velocity and shear are matched, the marginal curve of the rippling instability in figure 5(*a*) is not sensitive to details of the current profile, as long as the profile is smooth.

An important exception is provided by 'broken-line' velocity profiles used in many of the studies in the lower block of table 1, including Stern & Adam (1974). We have shown by comparison with the exponential profile, that broken-line profiles have very much greater growth rates than smooth profiles, even when there are so many broken line segments that the two velocity profiles are visually identical. And in the broken-line case the band of unstable wavenumbers is very much narrower than that of a visually identical smooth profile. In the broken-line case, the crucial second derivative U_{zz} is a set of δ-functions and is therefore qualitatively different from that of the
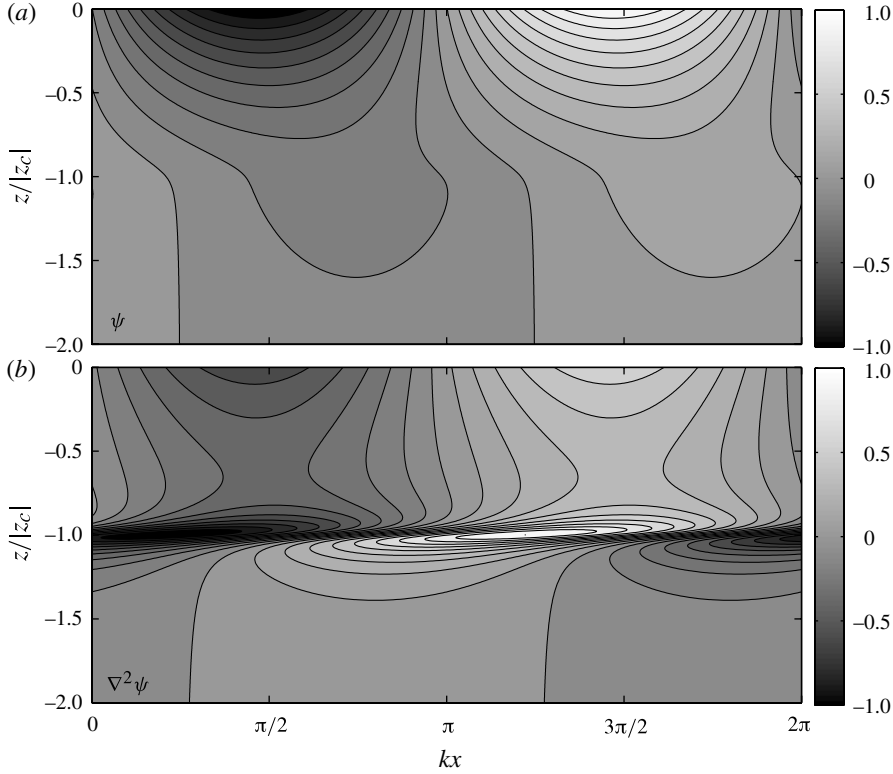
FIGURE 8. (*a*) The disturbance streamfunction ψ and (*b*) the vorticity $\zeta = \nabla^2\psi$ of an unstable mode. The parameters are $\bar{g} = 0.125$, $\bar{\gamma} = 0.01$ and $h_w k = 1.545$ (corresponding to the most rapidly growing wave); z_c is the depth of the critical level, i.e. in dimensional variables $c_r = U_s e^{z_c/\bar{h}_w}$. The plots are normalized to give a maximum value of unity and the contour interval is 0.1.

smooth profile. In particular, critical-level dynamics is seriously misrepresented. The differences are so strong that broken-line profiles must be regarded as very unreliable approximations to smooth profiles.

6. Approximations to the phase speed $c = c_r + \mathrm{i}c_i$ of the rippling mode

Continuing with $\epsilon = 0$, we turn now to the growth rate of the rippling mode and develop an approximation to the complex phase speed $c = c_r + \mathrm{i}c_i$. (This approximation is shown as the dotted curves in figure 4.) Our approach is close to the variational approximation of Miles (2001), which is motivated by the neutral solution of Morland *et al.* (1991) in (5.2). Thus we begin by considering a simple approximation to the exact $\Xi_w(c, k)$ in (4.9):

$$\Xi_w(c, k) \approx q(k)h_w^{-1}, \tag{6.1}$$

where we recall that $q(k) = \sqrt{1 + (h_w k)^2}$. We take the neutral solution, $\phi = \exp(qz/h_w)$, as a leading-order, non-irrotational approximate solution of Rayleigh's equation, even if $c \neq 0$.
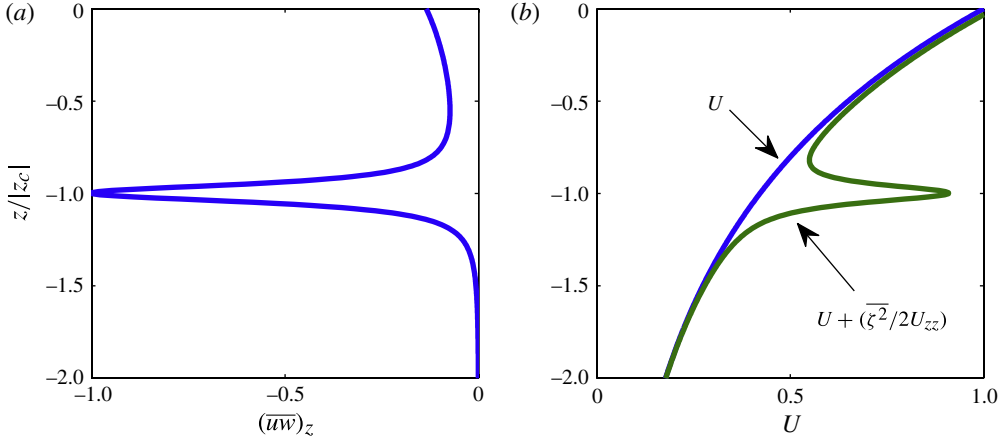
FIGURE 9. (Colour online) (*a*) The Reynolds stress divergence of the unstable wave in figure 8. (*b*) Modification of the base-state flow $U(z) = U_s \exp(z/h_w)$ by the Reynolds stresses in (*a*). To qualitatively illustrate the modification of the mean flow we assign a small amplitude to ζ.

6.1. *A first approximation to the dispersion relation*

With the approximate $\Xi_w(c, k)$ in (6.1), the $\epsilon = 0$ version of the surface boundary condition (2.15) is a quadratic equation for c, with solutions

$$c = c_{sgc}^-(k) \quad \text{and} \quad c = c_{sgc}^+(k), \tag{6.2}$$

where the 'sheared gravity–capillary' wave speeds are

$$c_{sgc}^\pm(k) \overset{\text{def}}{=} U_s \left[1 - \frac{1}{2q} \pm \sqrt{\frac{\bar{g} + \bar{\gamma} k^2}{q} + \frac{1}{4q^2}} \right], \tag{6.3}$$

where $\bar{g}$ and $\bar{\gamma}$ are non-dimensional parameters defined in (5.1). The dotted curves in figure 4(*a–c*) show that $c_{sgc}^-(k)$ is close to $c_r(k)$ of the rippling mode.

The designation of the dispersion relation (6.3) as 'gravity–capillary wave' comes from examination of the high-wavenumber limit of (6.3):

$$c_{sgc}^\pm(k) \to U_s \pm \begin{cases} \sqrt{g/k} & \text{if } \gamma = 0 \\ \sqrt{\gamma k} & \text{if } \gamma/(h_w U_s^2) > 0 \end{cases} \quad \text{as } k \to \infty. \tag{6.4}$$

In (6.4) the dispersion relation $c = c_{sgc}^\pm(k)$ is recognizable as the Doppler-shifted phase speed of gravity–capillary waves. The disturbance with speed c_{sgc}^+ is always travelling in the positive direction faster than U_s. Thus there can be no critical layer interaction between the fast c_{sgc}^+-wave and the current in the water. Instead, the c_{sgc}^+-wave has a critical layer in the fast flowing air. But because are considering $\rho_a = 0$, this critical level is inconsequential. In fact the c_{sgc}^+-wave is destabilized with a growth rate linearly proportional to ϵ (see §7 for further discussion of this Miles mode). On the other hand, we now show that the slow c_{sgc}^--wave is destabilized by critical-level resonance with the current in the water.

6.2. *Doppler shifting and critical-layer interactions*

The sheared gravity–capillary waves can satisfy the condition

$$0 < c_{sgc}^-(k) < U_s, \tag{6.5}$$

which is an analogue of the necessary condition for rippling instability in (4.10). Thus a critical-layer interaction between a c_{sgc}^--wave and the water current is possible. Interaction between a c_{sgc}^--wave and a critical layer in the water is the physical basis of the approximation developed in this section.

   This argument also indicates that surface tension plays a stabilizing role at high wavenumbers: short capillary waves travel quickly so that Doppler shifting cannot produce the necessary condition for instability in (6.5): this is evident in figure 4(c) where $c_r = 0$ at the high-wavenumber cut-off of the rippling instability. The high-wavenumber cut-off is a result of fast c_{sgc}^--capillaries overcoming the Doppler shift and propagating in their intrinsic (i.e. negative) direction against the base-state current.

6.3. *Why is the first approximation accurate even if $c_r/U_s = O(1)$?*

The success of the approximation $c_r(k) \approx c_{sgc}^-(k)$ in figure 4(a–c) encourages development of an improvement to the approximation (6.1) that delivers the imaginary part of the phase speed, i.e. the growth rate of the instability. But before undertaking this, one might ask why is the initial approximation (6.1) so effective? The $c = 0$ solution of Morland *et al.* (1991) in (5.2) is used to motivate (6.1), yet in figure 4(a,b) we see that $c_r(k) \approx c_{sgc}^-(k)$ works well even as $c_r \to U_s$. To better understand this triumph of perturbation theory, we write the non-dimensional water Rayleigh equation as

$$\phi_{\bar{z}\bar{z}} - q^2\phi = \frac{\bar{c}\phi}{\mathrm{e}^{\bar{z}} - \bar{c}} \tag{6.6}$$

where $\bar{z} \stackrel{\text{def}}{=} z/h_w$ and $\bar{c} \stackrel{\text{def}}{=} c/U_s$. Outside of the critical layer, the right-hand side of (6.6) is small relative to the left if $\bar{c}$ is small, or if q^2 is large. Examining figure 4, we see that when $\bar{c}_r = O(1)$, q^2 is large. In other words, the condition determining the validity of (6.1) is

$$\frac{|\bar{c}|}{q^2} \ll 1, \tag{6.7}$$

and this captures the entire unstable range.

6.4. *An improved approximation to the dispersion relation*

To improve (6.1), multiply (6.6) by $\mathrm{e}^{q\bar{z}}$ and integrate from $\bar{z} = -\infty$ to 0. One finds

$$\phi_{\bar{z}}(0) - q\phi(0) = \bar{c} \int_{-\infty}^0 \frac{\phi(\bar{z})\mathrm{e}^{q\bar{z}}}{\mathrm{e}^{\bar{z}} - \bar{c}} \, \mathrm{d}\bar{z}. \tag{6.8}$$

Now replace $\phi(\bar{z})$ on the right of (6.8) by $\phi(0)\exp(q\bar{z})$ to obtain

$$\Xi_w(k, c) \approx q\left(1 + \Omega\right), \tag{6.9}$$

where

$$\Omega(c, k) \stackrel{\text{def}}{=} \frac{\bar{c}}{q} \int_0^1 \frac{\xi^{2q-1}}{\xi - \bar{c}} \, \mathrm{d}\xi \tag{6.10}$$

is related to the dispersion function introduced by Miles (2001). Substituting (6.9) into the boundary condition (2.15) gives the improved dispersion relation, which in dimensional variables is

$$\left(c - c_{sgc}^+(k)\right)\left(c - c_{sgc}^-(k)\right) \approx -(c - U_s)^2 \Omega(c, k), \tag{6.11}$$

with the sheared gravity–capillary speeds, $c_{sgc}^\pm(k)$, given in (6.3).

Unfortunately $\Omega(c, k)$ in (6.10) cannot be evaluated in elementary terms: $\Omega(c, k)$ is a hypergeometric function. To obtain a simple approximation to the imaginary part of c, we use $c_r \approx c_{sgc}^-$ to further simplify (6.10) as

$$\frac{1}{\xi - (\bar{c}_r + \mathrm{i}\bar{c}_i)} \approx \mathrm{PV} \frac{U_0}{U_s \xi - c_{sgc}^-} + \mathrm{i}\pi U_0 \delta\left(U_s \xi - c_{sgc}^-\right), \tag{6.12}$$

where PV is 'principal value'. The Plemelj formula above requires $c_r \approx c_{sgc}^-$ and $0 < c_i \ll c_r$. Thus (6.10) becomes

$$\Omega \approx \frac{c_{sgc}^-}{q}\left(\mathrm{PV} \int_0^1 \frac{\xi^{2q-1}}{U_s \xi - c_{sgc}^-}\,\mathrm{d}\xi + \frac{\mathrm{i}\pi}{U_s}\left(\frac{c_{sgc}^-}{U_s}\right)^{2q-1}\right). \tag{6.13}$$

With the approximations made above, the factor $c - c_{sgc}^+$ on the left of (6.11) can be approximated by $c_{sgc}^- - c_{sgc}^+$, and thus finally

$$c \approx c_{sgc}^- + \frac{(c_{sgc}^- - U_s)^2}{c_{sgc}^+ - c_{sgc}^-}\frac{c_{sgc}^-}{q}\left(\mathrm{PV} \int_0^1 \frac{\xi^{2q-1}}{U_s \xi - c_{sgc}^-}\,\mathrm{d}\xi + \frac{\mathrm{i}\pi}{U_s}\left(\frac{c_{sgc}^-}{U_s}\right)^{2q-1}\right). \tag{6.14}$$

The imaginary part of (6.14) is elementary and is shown as the dotted curves in figure 4(*d–f*). This provides a tolerable approximation to c_i computed from the exact hypergeometric dispersion relation (2.15).

6.5. *Discussion of the approximate dispersion relation*

The approximation (6.14) is most accurate when c_r and c_i are both much less than U_s, and when $c_i \ll c_r$. These conditions are met on, and close to, the marginal curve in figure 5(*a*) and in this neighbourhood the approximation (6.14) is asymptotically valid. Numerical solution of the exact dispersion relation is most difficult where c_i is small and thus (6.14) is a useful complement to the hypergeometric solution. More importantly, the approximation (6.14) provides physical insight into the nature of this instability as an interaction between the sheared capillary–gravity wave c_{sgc}^- and a subsurface critical layer. The approximation identifies waves near the gravity–capillary transition as most likely to amplify via this rippling instability: disturbances with wavelength close to λ_{min} have the smallest phase speeds and are thus most easily Doppler shifted so that the resonance condition (6.5) is satisfied.

7. The Miles instability

7.1. *Expansion in $\epsilon \ll 1$*

We now show that the main properties of the prograde Miles mode in figures 2 and 3 follow from a regular expansion in powers of $\epsilon = \rho_a/(\rho_a + \rho_w)$. Begin by observing that the dispersion relation (2.15) can be written as

$$\mathscr{D}_0(c, k) + \epsilon \mathscr{D}_1(c, k) = 0, \tag{7.1}$$

where

$$\mathscr{D}_0(c,k) \overset{\text{def}}{=} \varXi_w(c,k)(c-U_s)^2 + S_0\,(c-U_s) - g - \gamma k^2, \tag{7.2}$$

$$\mathscr{D}_1(c,k) \overset{\text{def}}{=} [\varXi_a(c,k) - \varXi_w(c,k)]\,(c-U_s)^2 + S_1\,(c-U_s) + 2g. \tag{7.3}$$

In the above

$$S_0 = U_z(0^-) \quad \text{and} \quad S_1 = -U_z(0^-) - U_z(0^+). \tag{7.4}$$

An expansion of the solution, $c(k, \epsilon)$, as a regular perturbation series,

$$c(k, \epsilon) = c_0(k) + \epsilon c_1(k) + \cdots, \tag{7.5}$$

produces the leading-order balance

$$\mathscr{D}_0\,(c_0(k), k) = 0. \tag{7.6}$$

The problem (7.6) involves only the flow in the water. For the Miles mode, the relevant solution is the prograde mode, corresponding to the solid curve in figures 2(*a*) and 3(*a*). The phase speed of the prograde mode, $c_0(k)$, is always larger than the flow in the water: $c_0(k) > U_w(z)$. Thus there is no critical level in the water, and therefore no instability at leading order, i.e. the relevant solution of (7.6) is a forward Doppler-shifted capillary–gravity wave.

At $O(\epsilon)$ the expansion of the dispersion relation (7.1) results in

$$c_1 = -\frac{\mathscr{D}_1(c_0, k)}{\partial_c \mathscr{D}_0(c_0, k)}. \tag{7.7}$$

The instability is expressed via the imaginary part of c_1, e.g. as in (7.9) below. Using the hypergeometric solution of the double-exponential profile (4.1) we have verified the accuracy of the approximation (7.7). The approximate growth rate, that is $\epsilon k \operatorname{Im} c_1$, obtained from (7.7) is indistinguishable from the curves in figures 2(*b*) and 3(*b*). Figure 10 shows a further comparison in which the surface velocity U_s is varied with U_∞ fixed. Again, the approximation (7.7) is accurate to within the line width.

The Miles instability results from the air critical level at an altitude $z_c > 0$ determined by

$$c_0(k) = U(z_c). \tag{7.8}$$

The small growth rate of the prograde mode is obtained by taking the imaginary part of (7.7), which comes only from numerator. Using results from the Appendix, this imaginary part is

$$\operatorname{Im} \mathscr{D}_1 \approx (c_0 - U_s)^2 \pi \frac{U_c''}{|U_c'|} \frac{|\phi_c|^2}{|\phi_s|^2}, \tag{7.9}$$

where $U_c' = U_z(z_c)$, $U_c'' = U_{zz}(z_c)$, $\phi_c = \phi(z_c)$ and $\phi_s = \phi(0)$.

7.2. *The case $U_s = 0$*

The simplest illustration is the special case originally considered by Miles: $U_s = 0$ and $\gamma = 0$. Then $\varXi_w(c,k) = k$ and
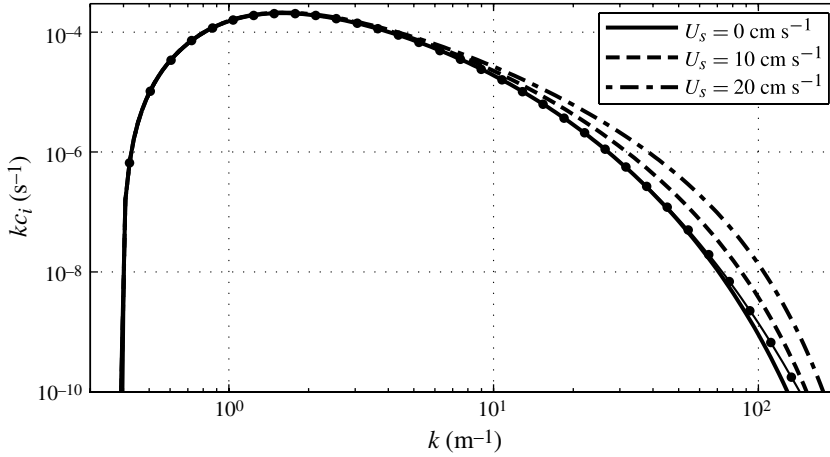
$$\mathscr{D}_0(c,k) = kc^2 - g. \tag{7.10}$$

FIGURE 10. The three curves indicated in the legend, with different values of surface velocity U_s, show the growth rate of the Miles mode computed from the complete dispersion relation (2.15) and also from (7.7) using analytic differentiation of the hypergeometric functions; the curves coincide to within the line width. Other parameters are $U_\infty = 5$ m s^{-1}, $h_a = 1$ m and $h_w = 2/k_{min} = 0.54$ cm. The thin curve with the dots superposed is the $U_s = 0$ growth rate computed from the approximation (7.15); the departure at large k is because (7.15) does not account for capillarity.

The leading-order solution is therefore $c_0(k) = \sqrt{g/k}$ and the results above imply that the growth rate, $\omega_i = \epsilon k \operatorname{Im} c_1$, is

$$\omega_i(k) = -\epsilon \sqrt{\frac{g}{k}} \frac{\pi}{2} \frac{U_c''}{|U_c'|} \frac{|\phi_c|^2}{|\phi_s|^2}. \tag{7.11}$$

This is Miles' classic result for the growth rate of surface gravity waves. Miles (1957) proceeded to estimate the factor $(|\phi_c|/|\phi_s|)^2$ in (7.11) using an *ad hoc* approximation. However Morland & Saffman (1993) showed that this further simplification of (7.11) results in an unreliable estimate of the growth rate.

In the particular case of the exponential velocity profile in (4.1), the critical-level condition (7.8) implies that

$$e^{-z_c/h_a} = 1 - \frac{1}{U_\infty} \sqrt{\frac{g}{k}} = 1 - \sqrt{\frac{m}{\kappa_a}}, \tag{7.12}$$

where

$$m \stackrel{\text{def}}{=} \frac{gh_a}{U_\infty^2} = h_a k_\infty \tag{7.13}$$

is the main control parameter of the Miles mode. Our goal is to characterize the growth rate of the Miles instability as a function of the non-dimensional wavenumber $\kappa_a = h_a k$ and the control parameter m.

We use the hypergeometric solution in (4.3) to evaluate the final factor in (7.11) and write the growth rate in (7.11) as

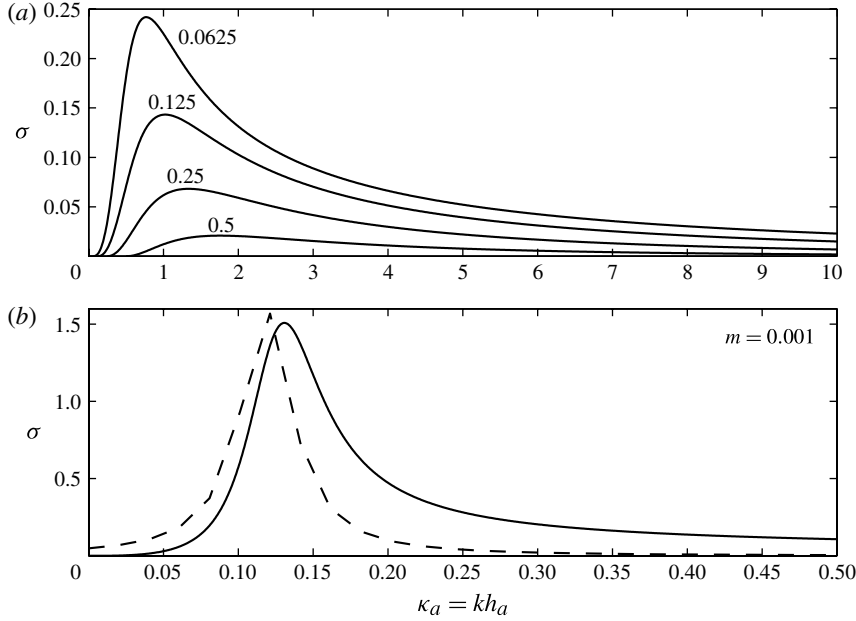$$\frac{h_a \omega_i}{\epsilon U_\infty} = \sigma(\kappa_a, m), \tag{7.14}$$

FIGURE 11. (*a*) The non-dimensional growth rate $\sigma(\kappa_a, m)$ in (7.15) as function of κ_a at four values of m indicated on the curves. The low-wavenumber cut-off is at $\kappa_a = m$. (*b*) A comparison of the small-m approximation (7.16) (the dashed curve) with the growth rate computed from (7.15) (the solid curve) at $m = 0.001$.

where the non-dimensional function $\sigma(\kappa_a, m)$ is

$$\sigma(\kappa_a, m) = \frac{\pi}{2}\sqrt{\frac{m}{\kappa_a}}\left(1 - \sqrt{\frac{m}{\kappa_a}}\right)^{2\kappa_a}\left[\frac{F(\alpha_a, \beta_a, 2\kappa_a + 1; 1)}{|F(\alpha_a, \beta_a, 2\kappa_a + 1; e^{z_c/h_a})|}\right]^2. \qquad (7.15)$$

The function $\sigma(\kappa_a, m)$ is shown in figure 11(*a*) for selected values of m. In figure 11(*a*) the low-wavenumber cutoff is at $\kappa_a = m$ (equivalent to $k = k_\infty$ in dimensional variables). There is no high-wavenumber cut-off: as $\kappa_a \to \infty$ the function σ in (7.15) is simplified asymptotically by replacing the final squared factor by one. Figure 12 shows the maximum growth rate, and the wavenumber of maximum growth computed from (7.15).

7.3. *The growth rate of the Miles instability as $m \to 0$*

Because of the factor $\epsilon \ll 1$ on the right of (7.14), the growth rate of the Miles instability for open-ocean waves (with lengths greater than a metre) is small, unless $m \ll 1$ and the base-state shear, U_∞/h_a, is large. For example, for the most unstable case shown in figures 2 and 3, $m = 0.15$ and $h_a/U_\infty = 0.125$ s, yet the e-folding time is in excess of 15 min. And in figure 10, with $m = 0.39$ and $h_a/U_\infty = 0.2$ s, the e-folding time is more than 3 h. Thus it is of interest to record an $m \to 0$ asymptotic simplification of (7.15):

$$\sigma(\kappa_a, m) \approx \frac{1}{2\pi m^{1/3}} \frac{(2\pi m^{2/3}/3)^2}{(2\pi m^{2/3}/3)^2 + (\kappa_a - \kappa_a^{max})^2}, \qquad (7.16)$$
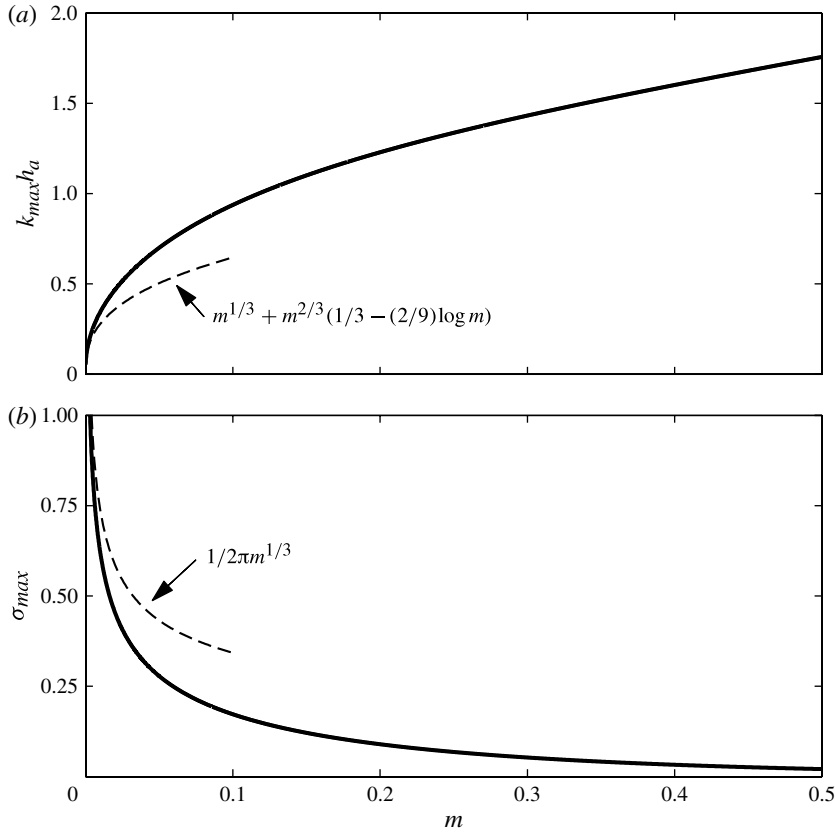
FIGURE 12. (*a*) The most unstable wavenumber as a function of *m* and (*b*) the maximum non-dimensional growth rate, $\sigma_{max}(m) = \sigma(h_a k_{max}, m)$. The dashed curves are the small-*m* approximations in (7.16) and (7.17).

where the wavenumber of maximum growth is

$$\kappa_a^{max} \stackrel{\text{def}}{=} m^{1/3} + m^{2/3}\left(\frac{1}{3} + \frac{2}{9}\ln\frac{1}{m}\right) + O\left(m\ln\frac{1}{m}\right). \tag{7.17}$$

We suppress the details of the hypergeometric asymptotics behind these formulae.

The main features of (7.16) and (7.17) are that for very small *m* the most unstable wavenumber is of order $m^{1/3}h_a^{-1}$ and the maximum growth rate is of order $\epsilon U_\infty/(m^{1/3}h_a)$. Figure 11(*b*) compares the approximation (7.16) to the growth rate computed from (7.15). The approximation (7.16) is accurate only for very small values of *m*, and then only for wavenumbers close to the wavenumber of maximum growth, i.e. κ_a values within $O(m^{2/3})$ of κ_a^{max}.

The results (7.16) and (7.17) are also subject to the restriction noted by Morland & Saffman (1993) that $m \geqslant \epsilon$ (or that the limit $\epsilon \to 0$ is taken before $m \to 0$). If instead $m \to 0$, with fixed ϵ, then the problem limits to Kelvin–Helmholtz instability and the approximation (7.5) is not valid.
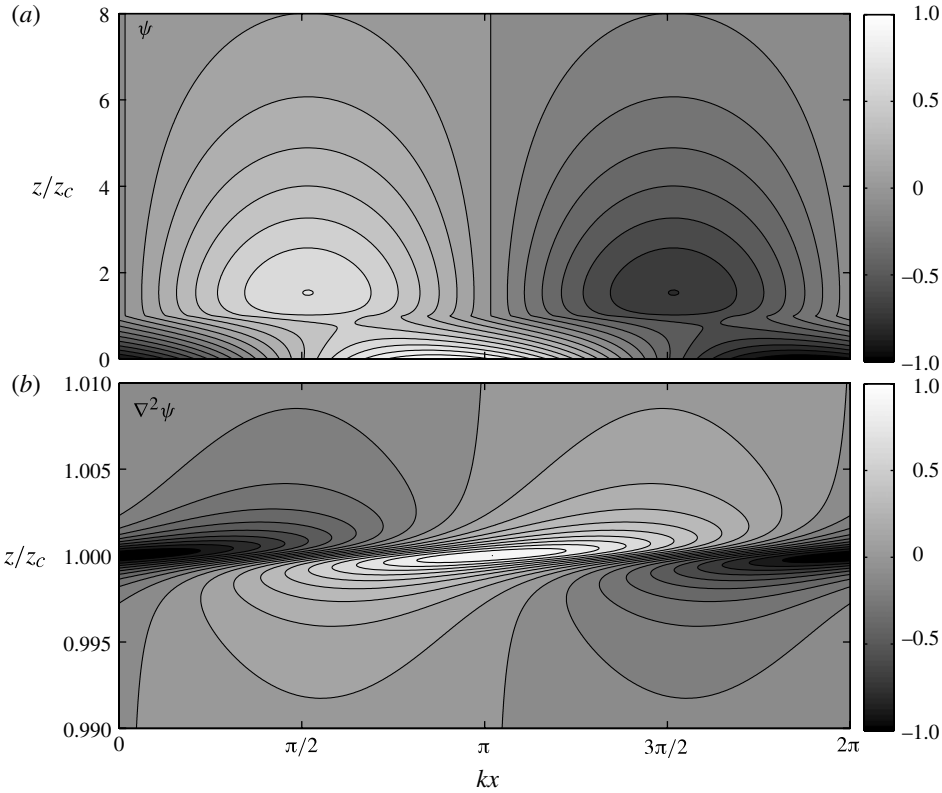
FIGURE 13. (*a*) The streamfunction in the air of the most rapidly growing Miles mode and (*b*) the vorticity in the vicinity of the critical level. This illustration shows the most rapidly growing mode on a shear flow with $U_s = 5$ m s^{-1} and $h_a = 0.255$ m (and therefore $m = 0.1$). The wavelength is 1.70 m, and the e-folding time, $(kc_i)^{-1}$, is 244 s. The phase speed is 1.63 m s^{-1} and the critical-level height is $z_c = 0.10$ m.

7.4. *The unstable Miles mode*

Figure 13 shows an unstable Miles mode in the air (the flow in the water is indistinguishable from an irrotational gravity wave). In figure 13(*a*) the critical level is evident as the region of rapid variation of the streamfunction. The critical layer is shown in an expanded view of the vorticity field in figure 13(*b*). The Reynolds stress of the disturbance vanishes above the critical level, i.e. the streamlines in figure 13(*a*) have the requisite tilt to produce a non-zero Reynolds correlation only below the critical level and above the wave crests.

Following the discussion of mean flow acceleration in §§ 3.2 and 3.3, the flow in the air is decelerated in the neighbourhood of the critical level and the momentum extracted from this critical layer is transferred into the zone below the wave crests and above the troughs. The deceleration in the critical layer is evident from the pseudomomentum formula (3.18): note that in the air $U_{zz} < 0$ at all heights, and therefore the induced mean flow, $\mathscr{U}(z, t)$, is necessarily negative. The momentum lost from the critical layer is balanced by the crest–trough momentum $\mathscr{I}_s$ in (3.10) and (3.12), i.e. the waves are 'pushed' as the air slows down. Notice that there is no

mean-flow acceleration in the water below the wave troughs: beneath the troughs the flow is irrotational and the Reynolds stress is therefore zero.

In terms of energetics, the first term in (3.22) is negligible because $\zeta = 0$ in the water. Thus the dominant energy balance of the unstable Miles mode is

$$(\rho_a + \rho_w)U_s \mathscr{J}_s + \widetilde{E} = \frac{1}{2} \int_0^\infty \rho_a \frac{\zeta^2 U}{|U_{zz}|} \ \mathrm{d}z. \qquad (7.18)$$

The terms on the left of (7.18) are the wave energy, $\widetilde{E}$, and the energy of the second-order mean flow in the crest–trough region. Both these left-hand terms are positive, and are balanced by the term on the right, which can be regarded as the atmospheric reservoir of base-state energy that is being tapped by the growing gravity wave.

8. Conclusion and discussion

We have a presented a unified discussion of the unstable modes on an air–water coupled shear flow. There are two types of unstable mode with very different properties: unstable ripples and the Miles mode. The wave–mean interaction of the two different unstable modes is explained in § 3 and provides a useful classification of the two instabilities.

Our main example has been the double-exponential velocity profile. At the technical level, it is now relatively easy to compute hypergeometric functions. Thus the double-exponential profile in (4.1), with its hypergeometric dispersion relation, might now be regarded as a canonical example. The double-exponential serves as an alternative to broken-line velocity profiles, which misrepresent critical-level dynamics and thus badly misjudge growth rates and the range of unstable wavenumbers.

A necessary condition for rippling instability is that the surface velocity U_s is faster than $c_{min} = 23$ cm s^{-1}, and once this condition is exceeded ripple growth is fast – see figures 2 and 7(b). Thus the rippling instability, if it is activated, will usually be the fastest growing mode. Detailed solution of the double-exponential stability problem delineates the stability boundary in the two-dimensional parameter space (as in figures 5 and 6), and provides the growth rate of the unstable ripples.

The growth of ripples results in an acceleration of the Eulerian mean current beneath wave troughs which is balanced by recoil in the above-trough region. The subsurface acceleration is greatest at the depth of the critical level. One might speculate that this mechanism may be a link in the chain of processes that move momentum out of an initial viscous wind-drift layer and into the deeper ocean. In this respect, Caponi *et al.* (1991) say of the rippling instability: 'a motivation for this work was the attempt to understand and explain simply some aspects of the generation of waves by wind, in particular the time for the appearance of relatively short waves and their phase speeds, when wind starts blowing over a flat calm, we have so far been unable to find concrete experimental data to support the prospect that this mechanism can play a primary role in wind-wave generation'.

But since 1991 experimental data have appeared and are not supportive of the speculations in the previous paragraph. For example, Melville, Shear & Veron (1998) show that the initial depth of the shear-layer profile increases as $\sqrt{\nu t}$, with ν the kinematic viscosity of water. This viscous process is first interrupted by the appearance of gravity–capillary waves with lengths of about one or two centimetres, and these ripples amplify very much faster than the $\sqrt{\nu t}$ deepening of the wind-drift layer. Langmuir circulations subsequently appear as a secondary instability of the surface wave field (Veron & Melville 2001). The $\sqrt{\nu t}$-shear profile – modelled by Melville

et al. (1998) using the error function and its relatives – is very similar to the exponential profile used here. However, in the laboratory, ripples first appear at surface speeds significantly less than 23 cm s^{-1}, e.g. in Veron & Melville (2001) ripples appear at a surface speed of $\sim$16 cm s^{-1}. We have no explanation for this significant difference between the laboratory and linear stability theory. This is, of course, not the only instance in which linear stability theory fails. But here the failure is particularly painful because of the compelling significance of c_{min} for the critical-layer problem.

It seems that the necessary condition for rippling, $U_s > c_{min}$, can be satisfied only in rather extreme conditions, such as the high-speed liquid jet realized experimentally by Itoh *et al.* (2007) or in the wake of a hydrofoil (Dimas & Triantafyllou 1994; Longuet-Higgins 1998). For ocean waves, our current understanding of generation is limited to the slowly growing Miles instability, which has been observed in the open ocean (Hristov *et al.* 2003). There is no comparable theory for the cat's paw ripples which soon form after a breeze starts to blow across a smooth flat sea surface.

Acknowledgements

Appendix. Properties of $\Xi_a(c,k)$ and $\Xi_w(c,k)$

Useful general expressions for Ξ_a and Ξ_w in (2.16) are obtained by multiplying the Rayleigh equation by $\phi^*(z)$ and integrating over the domain. Thus one finds that

$$\Xi_a(c,k) = \int_0^\infty |\phi_z|^2 + \left(k^2 + \frac{U_{zz}}{U-c}\right) |\phi|^2 \ \mathrm{d}z / |\phi_s|^2, \tag{A 1}$$

and

$$\Xi_w(c,k) = \int_{-\infty}^0 |\phi_z|^2 + \left(k^2 + \frac{U_{zz}}{U-c}\right) |\phi|^2 \ \mathrm{d}z / |\phi_s|^2, \tag{A 2}$$

where $\phi_s \stackrel{\text{def}}{=} \phi(0)$.

In §7 we need the imaginary part of $\Xi_a(c,k)$ in the case where $c_i \ll c_r$. In this event the denominator $U(z) - c$ in (A 1) results in a near-singularity at the critical level z_c defined via (7.8). A useful formula is obtained by taking the imaginary part of (A 1) and using

$$\lim_{c_i \downarrow 0} \frac{c_i U_{zz}}{(U-c_r)^2 + c_i^2} = \pi \frac{U'_c}{|U'_c|} \delta(z - z_c), \tag{A 3}$$

where $U'_c \stackrel{\text{def}}{=} U_z(z_c)$ and $U''_c \stackrel{\text{def}}{=} U_{zz}(z_c)$. Taking the imaginary part of (A 1) and using (A 3) we have

$$\lim_{c_i \downarrow 0} \text{Im} \ \Xi_a(c,k) = \pi \frac{U''_c}{|U'_c|} \frac{|\phi_c|^2}{|\phi_s|^2}, \tag{A 4}$$

where $\phi_c \stackrel{\text{def}}{=} \phi(z_c)$.

REFERENCES

BAKAS, N. & IOANNOU, P. 2009 Modal and nonmodal growths of inviscid planar perturbations in shear flows with a free surface. *Phys. Fluids* **21**, 024102.

BÜHLER, O. 2009 *Waves and Mean Flows*. Cambridge University Press.

CAPONI, E., CAPONI, M., SAFFMAN, P. & YUEN, H. 1992 A simple-model for the effect of water shear on the generation of waves by wind. *Proc. R. Soc. Lond.* A **438** (1902), 95–101.

CAPONI, E., YUEN, H., MILINAZZO, F. & SAFFMAN, P. 1991 Water-wave instability induced by a drift layer. *J. Fluid Mech.* **222**, 207–213.

DIMAS, A. A. & TRIANTAFYLLOU, G. S. 1994 Nonlinear-interaction of shear-flow with a free-surface. *J. Fluid Mech.* **260**, 211–246.

ENGEVIK, L. 2000 A note on the instabilities of a horizontal shear flow with a free surface. *J. Fluid Mech.* **406**, 337–346.

VAN GASTEL, K., JANSSEN, P. & KOMEN, G. 1985 On phase velocity and growth rate of wind-induced gravity–capillary waves. *J. Fluid Mech.* **161**, 199–216.

HRISTOV, T., MILLER, S. & FRIEHE, C. 2003 Dynamical coupling of wind and ocean waves through wave-induced air flow. *Nature* **422** (6927), 55–58.

HUGHES, T. H. & REID, W. H. 1965 On the stability of the asymptotic suction boundary-layer profile. *J. Fluid Mech.* **23**, 715–735.

ITOH, K., INOUE, M., KUMAMARU, H. & KUKITA, Y. 2007 Linear stability analysis on free-surface liquid jet with different simplification of velocity profile. *J. Fluid Sci. Technol.* **2** (2), 417–428.

JANSSEN, P. 2004 *The Interaction of Ocean Waves and Wind*. Cambridge University Press.

KAWAI, S. 1979 Generation of initial wavelets by instability of a coupled shear flows and their evolution to wind waves. *J. Fluid Mech.* **93**, 661–703.

LIGHTHILL, M. 1962 Physical interpretation of the mathematical theory of wave generation by wind. *J. Fluid Mech.* **14** (3), 385–398.

LIGHTHILL, M. 1978 *Waves in Fluids*. Cambridge University Press.

LONGUET-HIGGINS, M. S. 1998 Instabilities of a horizontal shear flow with a free surface. *J. Fluid Mech.* **364**, 147–162.

MELVILLE, W. K., SHEAR, R. & VERON, F. 1998 Laboratory measurements of the generation and evolution of langmuir circulations. *J. Fluid Mech.* **364**, 31–58.

MILES, J. W. 1957 On the generation of surface waves by shear flow. *J. Fluid Mech.* **3**, 185–204.

MILES, J. W. 1962 On the generation of surface waves by shear flow. Part 4. *J. Fluid Mech.* **13**, 433–448.

MILES, J. W. 2001 A note on surface waves generated by shear-flow instability. *J. Fluid Mech.* **447**, 173–177.

MORLAND, L. C. & SAFFMAN, P. G. 1993 Effect of wind-profile on the instability of wind blowing over water. *J. Fluid Mech.* **252**, 383–398.

MORLAND, L. C., SAFFMAN, P. G. & YUEN, H. C. 1991 Waves generated by shear layer instabilities. *Proc. R. Soc. Lond.* A **433** (1888), 441–450.

PHILLIPS, O. M. 1977 *The Dynamics of the Upper Ocean*. Cambridge University Press.

SHRIRA, V. I. 1993 Surface waves on shear currents: solution of the boundary-value problem. *J. Fluid Mech.* **252**, 565–584.

STERN, M. E. & ADAM, Y. A. 1974 Capillary waves generated by a shear current in water. In *Fifth Liège Colloquium on Ocean Hydrodynamics* (ed. J. Nihoul).

TAYLOR, G. I. 1915 Eddy motion in the atmosphere. *Phil. Trans. R. Soc. Lond.* **215**, 1–26.

VALENZUELA, G. 1976 The growth of gravity–capillary waves in a coupled shear flow. *J. Fluid Mech.* **76**, 229–250.

VERON, F. & MELVILLE, W. K. 2001 Experiments on the stability and transition of wind-driven water surfaces. *J. Fluid Mech.* **446**, 25–65.

WHELESS, G. & CSANADY, G. 1993 Instability waves on the air–sea interface. *J. Fluid Mech.* **248**, 363–381.

YIH, C.-S. 1972 Surface waves in flowing water. *J. Fluid Mech.* **51**, 209–220.

ZEISEL, A., STIASSNIE, M. & AGNON, Y. 2008 Viscous effect on wave generation by strong winds. *J. Fluid Mech.* **597**, 343–369.

ZHANG, X. 2005 Short surface waves on surface shear. *J. Fluid Mech.* **541**, 345–370.